The Astrophysical Journal, 890:90 (24pp), 2020 February 10 https://doi.org/10.3847/1538-4357/ab64eb

A Spectral Analysis of *Fermi*-LLE Gamma-Ray Bursts

Ming-Ya Duan[1,2] and Xiang-Gao Wang[1,2]
[1] GXU-NAOC Center for Astrophysics and Space Sciences, School of Physical Science and Technology, Guangxi University, Nanning 530004, People's Republic of China; wangxg@gxu.edu.cn
[2] Guangxi Key Laboratory for the Relativistic Astrophysics, Nanning 530004, People's Republic of China
Received 2019 June 23; revised 2019 December 19; accepted 2019 December 21; published 2020 February 14

Abstract

The prompt emission of gamma-ray bursts remains mysterious since the mechanism is difficult to understand even though there are many more observations with the development of detection technology. Most of the gamma-ray bursts spectra show the Band shape, which consists of the low-energy spectral index α, the high-energy spectral index β, the peak energy E_p, and the normalization of the spectrum. We present a systematic analysis of the spectral properties of 36 gamma-ray bursts (GRBs), which were detected by the Gamma-ray Burst Monitor (GBM) and simultaneously were also observed by the Large Area Telescope (LAT) and the LAT Low Energy (LLE) detector on the *Fermi* satellite. We performed a detailed time-resolved spectral analysis for all of the bursts in our sample. We found that the time-resolved spectrum at peak flux can be well fitted by the empirical Band function for each burst in our sample. Moreover, the evolution patterns of α and E_p have been carried for statistical analysis and the parameter correlations have been obtained such as E_p–F, α–F, and E_p–α, all of them are presented by performing a detailed time-resolved spectral analysis. We also demonstrated that the two strong positive correlations α–F and E_p–α for some bursts originate from nonphysical selection effects through simulation.

Unified Astronomy Thesaurus concepts: High-energy cosmic radiation (731); Astronomy data analysis (1858); Gamma-ray bursts (629)

1. Introduction

As we all know, gamma-ray bursts (GRBs) are the brightest explosions in the universe. It is generally believed that they are from magnetars or black holes resulting from the mergers of compact binaries (NS–NS or BH–NS) or the death of massive stars (Colgate 1974; Paczynski 1986; Eichler et al. 1989; Narayan et al. 1992; Woosley 1993; MacFadyen & Woosley 1999; Woosley & Bloom 2006; Kumar & Zhang 2015). The Band function (Band et al. 1993) can fit the gamma-ray burst spectra such as the time-integrated spectra and the time-resolved spectra, in which four parameters are contained: the low-energy power-law index α, the high-energy power-law index β, the peak energy E_p, and the normalized constant. It is proved that these parameters evolve with time instead of remaining constant. Many references, such as Golenetskii et al. (1983), Norris et al. (1986), Kargatis et al. (1994), Bhat et al. (1994), Ford et al. (1995), Crider et al. (1997), Kaneko et al. (2006), Peng et al. (2009) in the pre-*Fermi* era and Lu et al. (2012), Yu et al. (2016, 2019), Acuner & Ryde (2018), Li (2019) in the *Fermi* era have shown the evolutional characteristics of α and E_p in the Band function (Band et al. 1993). There are three types for the evolution patterns of peak energy E_p: (i) the "hard-to-soft" trend, when the value of E_p decreases monotonically (Norris et al. 1986; Bhat et al. 1994; Band 1997); (ii) those varying with flux, i.e., E_p will increase/decrease since the flux is increasing/decreasing, called the "flux-tracking" trend (Golenetskii et al. 1983; Ryde & Svensson 1999); (iii) the "soft-to-hard" trend or chaotic evolutions (Laros et al. 1985; Kargatis et al. 1994). Recently, Lu et al. (2012) and Yu et al. (2019) pointed out that the first two patterns are dominant. For the evolution of the low-energy photon index α, it does not show a strong general trend compared with E_p, although it evolves with time instead of remaining constant. However, the physical origin of the evolution patterns in E_p and α is not very clear. On the other hand, the analysis of a large sample of LLE GRBs for the parameters evolution and the parameter correlations is lacking, except for the single burst analysis, such as GRB 131231A in Li et al. (2019), which is a single-pulse burst, and GRB 180720B in Duan & Wang (2019), which is a multi-peaked burst in the prompt light curve.

Furthermore, the launch of the *Fermi Space Gamma-ray Telescope* (*Fermi*) in 2008 (Atwood et al. 2009) makes it possible to detect GRBs in a broad energy band both in the prompt emission and the afterglow phase. The *Fermi* satellite consists of the Gamma-ray Burst Monitor (GBM) and the Large Area Telescope (LAT) with the LAT Low Energy (LLE) detector. The GBM consists of 12 NaI detectors (8–900 keV) and two BGO (200 keV–40 MeV) detectors. Obviously, the energy range in GBM detection is from 8 keV to 40 MeV. The LAT can detect photons with an energy range from 100 MeV to 300 GeV. Moreover, the LLE can collect lower energy gamma-ray photons down to 10 MeV. About 2000 GRBs have been detected by *Fermi* in the last ten years while fewer of them were detected by *Fermi*-LAT, with the number just more than 100. In addition, GRBs detected by LLE are fewer than 100 according to the available data at the Fermi Science Support Center (FSSC).[3] Ajello et al. (2019) note that only 74 GRBs were co-detected by the GBM and LAT (including LAT-LLE). We call them LLE GRBs. The photons cover eight orders of magnitude in the energy range for LLE bursts.

In this work, after performing a detailed time-resolved spectral analysis of the bright gamma-ray bursts with the detection of *Fermi*-LLE in the prompt phase, we present the time-resolved spectra around their peak flux, for which they all can be fitted well by the Band function. Then we give the evolution patterns of the peak energy E_p and low-energy

[3] https://fermi.gsfc.nasa.gov/ssc/data/access/

Table 1
Results of the Time-resolved Spectral Fits at Peak Flux for All Samples

GRB	$t_1 \sim t_2$ (s)	α	β	E_p (keV)	Red.χ^2
(1)	(2)	(3)	(4)	(5)	(6)
080825C	2.978∼3.937	-0.4269 ± 0.0924	-2.105 ± 0.102	205.1 ± 19.5	0.96
090328A	23.705∼25.400	-0.9062 ± 0.0500	-2.220 ± 0.192	444.0 ± 57.2	1.15
090626A	34.580∼35.053	-0.7057 ± 0.0541	-2.530 ± 0.239	324.7 ± 27.3	0.92
090926A	4.129∼4.326	-0.3629 ± 0.0699	-2.048 ± 0.055	249.5 ± 18.7	0.97
100724B	61.818∼62.852	-0.6834 ± 0.0469	-1.936 ± 0.060	517.2 ± 52.6	1.09
100826A	20.799∼21.574	-0.7023 ± 0.0461	-2.033 ± 0.072	536.0 ± 53.3	1.12
101014A	0.961∼1.288	-0.4757 ± 0.0542	-2.334 ± 0.101	281.6 ± 18.0	1.02
110721A	0.889∼1.660	-0.8542 ± 0.0321	-2.111 ± 0.095	1236.0 ± 145	1.18
120226A	17.503∼19.860	-0.7359 ± 0.0857	-1.805 ± 0.063	238.4 ± 37.3	1.04
120624B	11.963∼14.037	-0.9411 ± 0.0443	-2.174 ± 0.172	611.3 ± 85.0	0.88
130502B	20.322∼20.586	-0.1871 ± 0.0530	-2.829 ± 0.199	320.3 ± 15.0	0.95
130504C	31.005∼31.342	-0.8189 ± 0.0500	-1.938 ± 0.070	705.9 ± 97.9	1.00
130518A	25.899∼26.280	-0.8515 ± 0.0394	-2.172 ± 0.075	567.6 ± 51.3	0.97
130821A	30.039∼30.936	-0.6272 ± 0.0733	-1.898 ± 0.055	246.9 ± 27.3	0.99
131108A	0.000∼1.257	-0.6219 ± 0.0672	-1.871 ± 0.040	341.0 ± 34.6	0.98
140102A	2.281∼2.635	-0.6150 ± 0.0710	-2.099 ± 0.075	223.4 ± 20.5	0.93
140206B	13.522∼13.968	-0.5438 ± 0.0569	-2.142 ± 0.079	336.6 ± 26.7	1.02
141028A	12.028∼13.363	-0.6414 ± 0.0555	-2.111 ± 0.103	416.2 ± 40.0	0.97
150118B	45.747∼46.332	-0.5728 ± 0.0329	-3.067 ± 0.316	881.3 ± 53.4	0.96
150202B	8.063∼8.789	-0.7736 ± 0.0612	-1.872 ± 0.070	383.2 ± 53.8	1.07
150314A	1.254∼1.549	-0.3399 ± 0.0448	-2.462 ± 0.088	413.5 ± 19.8	1.03
150403A	10.798∼11.410	-0.6775 ± 0.0418	-2.059 ± 0.074	639.9 ± 59.6	1.11
150510A	0.000∼0.564	-0.6889 ± 0.0275	unconstrained	1141.0 ± 65.9	0.97
150627A	59.694∼59.961	-0.8258 ± 0.0441	-2.627 ± 0.228	317.8 ± 24.3	0.87
150902A	9.046∼9.291	-0.3920 ± 0.0471	-2.587 ± 0.142	411.5 ± 22.7	0.98
160509A	13.795∼14.005	-0.5605 ± 0.0573	-2.077 ± 0.069	336.7 ± 28.7	0.91
160816A	8.023∼8.304	-0.0321 ± 0.0625	-3.032 ± 0.287	322.8 ± 15.0	0.91
160821A	135.76∼135.87	-0.9698 ± 0.0376	-1.776 ± 0.054	1093.0 ± 192.0	1.12
160905A	12.267∼13.725	-0.7799 ± 0.0423	-2.197 ± 0.113	987.2 ± 120.0	1.15
160910A	8.235∼8.477	-0.2183 ± 0.0540	-2.332 ± 0.072	370.8 ± 19.8	0.94
170115B	0.000∼1.361	-0.5548 ± 0.0284	-3.430 ± 0.423	1931.0 ± 102.0	1.04
170214A	60.990∼62.311	-0.6362 ± 0.0650	-1.821 ± 0.050	360.1 ± 41.8	0.96
170510A	17.310∼19.347	-0.8697 ± 0.0543	-2.052 ± 0.121	433.2 ± 57.5	0.91
170808B	16.383∼16.472	-0.8287 ± 0.0341	-3.215 ± 0.447	514.0 ± 33.0	0.91
171210A	3.647∼5.265	-0.7582 ± 0.0415	-2.960 ± 0.658	572.5 ± 49.8	0.96
180305A	3.334∼4.174	-0.0916 ± 0.0525	-3.172 ± 0.461	502.8 ± 24.1	1.00

spectral index α. The parameter correlations will also be presented in our analysis such as E_p–F, α–F, and E_p–α. Besides, we will make a statistical analysis for whether the low-energy power-law indices α exceed the synchrotron limit ($\alpha = -\frac{2}{3}$) given by Preece et al. (1998) in these slices. We will perform a simulation to identify whether the two strong positive correlations α–F and E_p–α for some bursts are intrinsic or artificial.

2. Sample Selection and Method

Up to now, more than one hundred bursts have been co-detected by the *Fermi*/GBM and LAT, but only 74 GRBs (Ajello et al. 2019) were detected by LLE, which can collect those lower energy gamma-ray photons down to 10 MeV in all of these bursts if there is no omission in our collection. This work makes use of all available LLE bursts observed until 2018 July 20. We remove a pure blackbody burst GRB 090902B, three extremely bright bursts (GRBs 080916C, 130427A and 160625B) and two long bursts that have been studied in Li et al. (2019) (GRB 131231A) and Duan & Wang (2019) (GRB 180720B) in detail. These two long bursts originate from synchrotron emission in the prompt phase.

We downloaded data from the FSSC as described above. To complete this study, we take RMFIT as the tool for making the time-resolved spectral analysis. We perform a detailed time-resolved spectral analysis by using the TTE event data files of two Na I detectors and the corresponding BGO detector(s) on *Fermi*/GBM, but the use of LAT and LLE data was abandoned because of their lower impact for peak energy E_p and low-energy spectral index α. The background photon counts were estimated by fitting the light curve before and after the operated burst with a one-order background polynomial model. We selected all of the prompt phase as the source. We take the signal-to-noise ratio (S/N) as 40 in all of the slices for each burst and they all can be well fitted by the Band function (Band et al. 1993). To show the spectral evolution, the sample in our analysis includes only those bursts from which at least five time-resolved spectra can be produced from the data. Based on this, 32 GRBs have been excluded due to the insufficiency of the number of time-resolved spectra. Finally, we get a sample of 36 GRBs by filtering described as above. The reduced χ^2 has been taken into measuring the goodness of fit (GoF). The χ^2/GoF is typically in the range of 0.75–1.5 in each slice.

In our work, we present the Band-fitting spectra for all of the bursts around their peak flux first. For the evolution patterns of

Table 2
Results of the Time-integrated Spectral Fits for All Samples

GRB	z	T_{90} (s)	$t_1 \sim t_2$[a] (s)	α	β	E_p (keV)	Red.χ^2
(1)	(2)	(3)	(4)	(5)	(6)	(7)	(8)
080825C	...	22	0 ∼ 30.016	−0.6197 ± 0.0595	−2.243 ± 0.119	174.7 ± 11.6	1.14
090328A	0.736	80	0 ∼ 80.064	−1.1790 ± 0.0294	−2.352 ± 0.366	756.0 ± 121.0	1.19
090626A	...	70	0 ∼ 70.016	−1.1920 ± 0.0448	−2.061 ± 0.074	152.2 ± 15.8	1.10
090926A	2.106	20	0 ∼ 25.024	−0.7967 ± 0.0108	−2.428 ± 0.054	312.4 ± 6.1	1.97
100724B	...	111.6	0 ∼ 100.031	−0.7046 ± 0.0251	−1.904 ± 0.035	384.6 ± 19.3	1.38
100826A	...	100	0 ∼ 100.032	−0.8828 ± 0.0224	−1.897 ± 0.029	289.4 ± 14.4	2.03
101014A	...	450	0 ∼ 50.047	−1.1690 ± 0.0190	−2.470 ± 0.128	186.7 ± 8.1	1.46
110721A	0.382	24.45	0 ∼ 30.015	−1.0790 ± 0.0343	−1.742 ± 0.035	411.1 ± 56.3	1.10
120226A	...	57	0 ∼ 60.032	−0.9439 ± 0.0390	−2.008 ± 0.090	266.1 ± 25.1	1.27
120624B	2.20	271	0 ∼ 30.016	−0.9902 ± 0.0328	−2.505 ± 0.383	685.4 ± 78.3	1.13
130502B	...	24	0 ∼ 35.006	−0.6279 ± 0.0129	−2.404 ± 0.051	303.8 ± 5.9	1.83
130504C	...	74	0 ∼ 80.064	−1.2830 ± 0.0114	−2.250 ± 0.110	858.8 ± 66.4	1.45
130518A	2.49	48	0 ∼ 50.045	−0.8689 ± 0.0157	−2.288 ± 0.055	408.5 ± 13.5	1.38
130821A	...	84	0 ∼ 100.031	−1.1860 ± 0.0226	−2.044 ± 0.073	317.3 ± 26.4	1.78
131108A	2.4	19	0 ∼ 25.024	−0.9453 ± 0.0253	−2.337 ± 0.104	381.0 ± 20.6	1.07
140102A	...	65	0 ∼ 30.015	−1.2550 ± 0.0300	unconstrained	211.2 ± 13.2	1.21
140206B	...	120	0 ∼ 55.039	−1.0260 ± 0.0158	−2.041 ± 0.032	271.9 ± 10.6	2.11
141028A	2.332	31.5	0 ∼ 35.008	−0.6429 ± 0.0415	−1.884 ± 0.037	254.9 ± 16.0	1.16
150118B	...	40	0 ∼ 50.048	−0.8896 ± 0.0098	−3.435 ± 0.439	743.1 ± 20.5	1.42
150202B	...	167	0 ∼ 50.048	−0.7537 ± 0.0440	−2.260 ± 0.166	235.0 ± 17.7	1.23
150314A	1.758	14.79	0 ∼ 20.032	−0.8268 ± 0.0104	−2.897 ± 0.136	404.7 ± 7.9	1.55
150403A	2.06	40.9	0 ∼ 50.046	−0.7383 ± 0.0266	−1.986 ± 0.044	312.8 ± 15.6	1.18
150510A	...	52	0 ∼ 60.032	−1.0530 ± 0.0104	unconstrained	1640.0 ± 82.4	1.27
150627A	...	65	0 ∼ 80.063	−1.0660 ± 0.0104	−2.154 ± 0.030	239.4 ± 6.1	2.49
150902A	...	14	0 ∼ 20.032	−0.7066 ± 0.0125	−2.480 ± 0.063	431.9 ± 9.5	1.62
160509A	1.17	371	0 ∼ 50.047	−0.8953 ± 0.0107	−2.041 ± 0.024	373.2 ± 9.8	1.92
160816A	...	14	0 ∼ 20.032	−0.7409 ± 0.0215	−3.350 ± 0.492	235.8 ± 6.7	1.14
160821A	...	120	109.952 ∼ 170.048	−1.0680 ± 0.0034	−2.299 ± 0.021	966.3 ± 14.9	⋯
160905A	...	64	0 ∼ 80.064	−1.0950 ± 0.0174	−2.844 ± 0.359	1392.0 ± 143.0	1.82
160910A	...	24.3	0 ∼ 30.016	−0.9891 ± 0.0126	−1.776 ± 0.012	506.9 ± 22.2	3.86
170115B	...	44	0 ∼ 50.048	−0.8061 ± 0.0239	−2.504 ± 0.156	997.4 ± 65.6	2.39
170214A	2.53	123	0 ∼ 150.016	−0.9511 ± 0.0133	−2.519 ± 0.137	465.7 ± 16.1	2.03
170510A	...	128	0 ∼ 135.040	−1.2760 ± 0.0315	unconstrained	563.2 ± 84.9	1.47
170808B	...	17.7	0 ∼ 25.024	−0.9949 ± 0.0101	−2.297 ± 0.035	249.1 ± 5.2	2.28
171210A	...	143	0 ∼ 145.024	−0.7107 ± 0.0383	−2.244 ± 0.063	136.3 ± 5.6	1.30
180305A	...	12.5	0 ∼ 15.040	−0.3126 ± 0.0266	−2.490 ± 0.098	329.5 ± 9.6	1.27

Note.
[a] Time intervals.

α and E_p we will then identify them as "hard-to-soft" (h.t.s.), "soft-to-hard" (s.t.h.), "intensity-tracking" (i.t.), "rough-tracking" (r.t.), "anti-tracking" (a.t.), and "no", which means that it evolves without rule. It is notable that all "-tracking" patterns are based on the evolution of the energy flux. Finally, the statistical analysis of the linear dependence in the parameter correlations such as E_p–F, α–F, and E_p–α will be made by using Pearson's correlation coefficient r. We also address whether the two observed correlations α–F and E_p–α are intrinsic or artificial by simulation.

3. Data Analysis and Results

The data analysis results have been presented in Tables 1–3, Figures 1–11. Table 1 shows the results of the time-resolved spectral fits at peak flux for all samples. Table 2 shows the results of the time-integrated spectral fits for all samples. The fitting results of the parameter correlations and the spectral evolution patterns of α and E_p have been shown in Table 3; simultaneously we also present the linear-fitting results from simulations for those bursts (23 GRBs) that exhibit a strong positive correlation in α–F and E_p–α correlations in this table. Figure 1 is a histogram of the maximal value of α in the detailed time-resolved spectra for each burst. Figure 2 presents those spectra with the best Band-fitting results around the peak flux for all of our bursts. Figure 3 shows a comparison between our fitting results and the results of the GBM catalog (Gruber et al. 2014; Narayana Bhat et al. 2016) at peak flux. Figure 4 presents a comparison between the histogram of α in the time-integrated spectra in our energy range and the BATSE energy range. Figure 5 shows a comparison between our time-integrated spectral analysis results and the corresponding results of the GBM catalog (Gruber et al. 2014). Figure 6 represents the temporal characteristics of energy flux for all bursts in our sample (the left-hand y-axis), along with the time evolution of E_p and α; both are marked with red stars in the right-hand y-axis. That is to say, Figure 6 shows the spectral evolutions for all of the bursts in our sample. The histograms of E_p and α obtained by performing a detailed time-resolved spectral analysis have been shown in Figure 7. The correlations such as E_p–F, α–F, and E_p–α obtained from the time-resolved

Table 3
Fitting Results of the Parameter Correlations and the Spectral Evolutions of E_p and α

GRB	Detectors	N	E_p–F r	α–F r	E_p–α r	Spectral Evolutions E_p/α	$\alpha > -\frac{2}{3}$	α–F r(S)	E_p–α r(S)
(1)	(2)	(3)	(4)	(5)	(6)	(7)	(8)	(9)	(10)
080825C	n9,na,b1	8	0.94	0.70	0.54	h.t.s./r.t.	yes	−0.38	−0.96
090328A	n7,n8,b1	8	0.70	0.93	0.83	h.t.s./i.t.	no	−0.20	−0.86
090626A	n0,n3,b0	20	0.61	0.69	0.01	r.t./r.t.	not all	−0.56	−0.88
090926A	n6,n7,b1	37	0.61	0.67	0.35	r.t./r.t.	not all	−0.36	−0.86
100724B	n0,n1,b0	30	0.59	0.35	−0.08	r.t./r.t.	not all	⋯	⋯
100826A	n7,n8,b1	24	0.93	0.08	−0.01	r.t./r.t.	not all	⋯	⋯
101014A	n6,n7,b1	21	0.86	0.83	0.62	r.t./r.t.	not all	0.28	−0.54
110721A	n6,n9,b1	7	0.62	0.76	0.07	h.t.s./s.t.h. to h.t.s.	no	−0.71	−0.88
120226A	n0,n1,b0	12	0.47	0.73	−0.11	r.t./r.t.	no	−0.57	−0.87
120624B	n1,n2,b0	5	0.52	0.61	0.94	h.t.s./h.t.s.	no	−0.40	−0.80
130502B	n6,n7,b1	25	0.64	0.75	0.24	r.t./r.t.	not all	−0.13	−0.67
130504C	n9,na,b1	29	0.54	0.45	−0.18	r.t./r.t.	no	⋯	⋯
130518A	n3,n7,b0,b1	19	0.61	0.69	0.32	r.t./r.t.	no	−0.71	−0.81
130821A	n6,n9,b1	11	0.67	0.71	−0.06	r.t./r.t.	not all	−0.002	−0.95
131108A	n3,n6,b0,b1	6	0.84	0.77	0.44	s.t.h. to h.t.s./r.t.	not all	−0.14	−0.32
140102A	n7,n9,b1	6	0.89	0.84	0.71	i.t./i.t.	not all	−0.002	−0.93
140206B	n0,n1,b0	23	0.67	0.58	0.38	r.t./r.t.	not all	⋯	⋯
141028A	n6,n9,b1	5	0.91	−0.07	0.18	i.t./h.t.s.	yes	⋯	⋯
150118B	n1,n2,b0	20	0.86	0.50	0.26	r.t./r.t.	not all	⋯	⋯
150202B	n0,n1,b0	7	0.72	−0.48	−0.69	r.t./a.t.	not all	⋯	⋯
150314A	n1,n9,b0,b1	17	0.05	0.95	0.05	no/r.t.	not all	−0.64	−0.89
150403A	n3,n4,b0	9	0.83	0.39	0.01	r.t./r.t.	not all	⋯	⋯
150510A	n0,n1,b0	11	0.56	0.95	0.55	s.t.h. to h.t.s./r.t.+h.t.s.	not all	0.27	−0.86
150627A	n3,n4,b0	39	0.66	0.75	0.59	r.t./r.t.	not all	−0.45	−0.79
150902A	n0,n3,b0	17	0.58	0.85	0.29	r.t./r.t.	not all	−0.68	−0.91
160509A	n0,n3,b0	39	0.46	0.83	0.39	r.t./r.t.	not all	−0.18	−0.96
160816A	n6,n7,b1	10	0.76	0.70	0.27	i.t./r.t.	not all	−0.08	−0.64
160821A	n6,n7,b1	130	0.43	0.81	0.08	r.t./r.t.	no	0.07	−0.72
160905A	n6,n9,b1	12	0.71	0.97	0.73	r.t./r.t.	no	0.65	−0.76
160910A	n1,n5,b0	13	0.83	0.17	−0.06	h.t.s./no	not all	⋯	⋯
170115B	n0,n1,b0	5	0.99	−0.95	−0.97	i.t./a.t.	yes	⋯	⋯
170214A	n0,n1,b0	24	0.30	0.73	−0.18	r.t./r.t.	not all	−0.64	−0.90
170510A	n9,na,b1	7	0.16	0.82	−0.02	no/r.t.	no	−0.43	−0.84
170808B	n1,n5,b0	31	0.81	0.33	0.27	r.t./r.t.	not all	⋯	⋯
171210A	n0,n1,b0	17	0.90	−0.50	−0.56	r.t.+h.t.s./no	not all	⋯	⋯
180305A	n1,n2,b0	8	0.83	−0.31	0.02	i.t./no	yes	⋯	⋯

spectra are shown in Figure 8. Figure 9 shows the histograms of Pearson's correlation coefficient from the fitting results of parameter correlations such as E_p–F, α–F, and E_p–α. The last two figures, Figures 10, 11, are the linear-fitting results in α–F and E_p–α correlations from simulation for 23 GRBs.

3.1. Band-fitting Results at Peak Flux for All of the Bursts

We have extracted the maximal value of α after performing a detailed time-resolved spectral analysis for each burst (Figure 1). The fact that most of them (77.8%) in our sample are larger than the synchrotron limit, which is the value of $-\frac{2}{3}$, is amazing. Historically, it was thought that the fitted spectrum cannot be produced by synchrotron emission when the spectral slope $\alpha \geqslant -\frac{2}{3}$. However, the recent study in Burgess et al. (2019) showed that the synchrotron model can fit most of the bursts with the Band α parameter harder than the line-of-death limit. Additionally, Lundman et al. (2013) pointed out that some structured jet photosphere models can also account for slopes softer than $-\frac{2}{3}$ even though in the majority of cases it is not easy to do so (Deng & Zhang 2014). Burgess et al. (2014) illustrated that the Band function cannot be representative of a nonthermal synchrotron emission component because the blackbody component will be more significant when a physical synchrotron model is used to perform the spectral fitting analysis instead of the Band function. Based on the above, it seems difficult to identify whether they originated from the synchrotron emission or photosphere model. Also, it is difficult to address the question whether the thermal component was detected in each burst. Perhaps the spectral information at peak flux is representative among all the time-resolved spectra. In this section, we present the spectra with the best Band-fitting results at peak flux for all of our bursts in Figure 2. Correspondingly, the GRB name, the fitting interval, as well as the fitting results such as α, β, E_p, and the reduced χ^2 are listed in Table 1. Undoubtedly, a single Band function is enough to perform a spectral fitting for every burst from those fitting lines in Figure 2 even though there are papers that argued that the blackbody component was detected in some bursts such as GRB 100724B (Guiriec et al. 2011), GRB 110721A (Axelsson et al. 2012; Zhang et al. 2012), and so on.

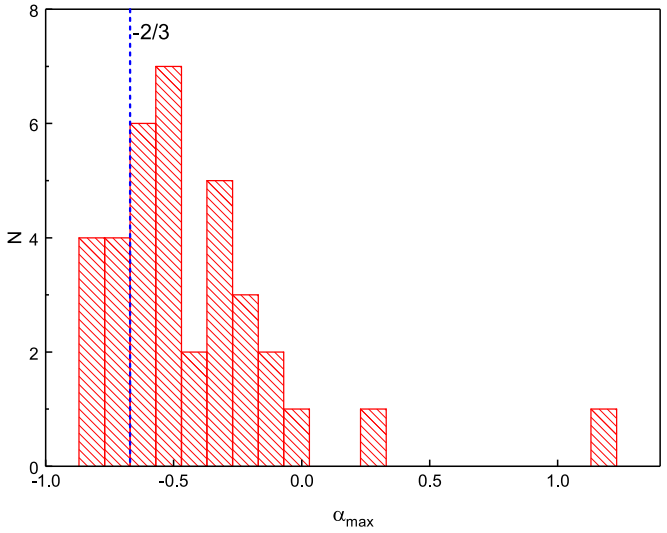

Figure 1. Histogram of the maximal value of α in the detailed time-resolved spectra for each burst. The blue short dashed line indicates the synchrotron limit ($-\frac{2}{3}$). One can see that 77.8% of the bursts have an α_{max}, which is larger than the synchrotron limit in our sample of bursts.

Additionally, we found that the maximal value of the low-energy spectral index α_{max} in the time-resolved spectra is equal to the value of α around the peak flux for seven GRBs (GRBs 080825C, 101014A, 130821A, 131108A, 140102A, 150510A, 160816A) due to the fact that the value of α is maximal while the peak flux is emerging. For the rest of the bursts, the maximal value of α is larger than the value of α at peak flux. Especially, the two values are vastly different for seven GRBs (GRBs 090626A, 100826A, 141028A, 150627A, 170115B, 170808B, 171210A); the α_{max} is much larger than the value of α at peak flux for them.

Since we used RMFIT to fit the GRB spectra, we also compared the results in our sample with those published in the *Fermi* GRB spectral catalogs such as Gruber et al. (2014) and Narayana Bhat et al. (2016). In Figure 3, the distributions of the low-energy spectral indices, high-energy spectral indices, peak energy E_p, energy flux, photon flux, and energy fluence obtained from our time-resolved spectral fits at peak flux are shown in red dashed–dotted–dotted lines. Meanwhile, the blue short dashed–dotted lines show the corresponding distributions in Gruber et al. (2014) or Narayana Bhat et al. (2016). The BEST sample that was fitted by the Band function (in short, the BEST-Band sample) in Gruber et al. (2014) was used for comparison. The energy flux, photon flux, and energy fluence are in the energy range from 10 keV to 1 MeV. The values of α are in the interval from -1 to 0 for the two distributions (although they have different distribution structures and peaks), which peak around -0.7 ± 0.1 (LLE bursts) and -0.5 ± 0.1 (BEST-Band sample), respectively. For the β distribution, from -2.8 to -1.8, they are 75% (LLE bursts) and 92% (BEST-Band sample), respectively. It is obvious that the peak energies have a median value of around 500 keV (LLE sample) and 200 keV (BEST-Band sample), respectively. Especially, 55.6% of the LLE bursts have an E_p value that is larger than 400 keV, and only 12% of the BEST-Band bursts have an E_p with the value of >400 keV. The energy flux values are larger than 1×10^{-6} erg cm^{-2} s^{-1} both for the LLE sample and BEST-Band sample. We find that 94.4% of the LLE bursts and 92% of the BEST-Band bursts are in the interval from 1×10^{-6} to 2.5×10^{-5} erg cm^{-2} s^{-1}. For the distributions of photon flux and energy fluence, all of the bursts in Narayana Bhat et al. (2016) (1405 GRBs) have been selected (see the two bottom panels in Figure 3). The distribution of photon flux covers an interval from 0.8 to 1000 photons cm^{-2} s^{-1} based on these 1405 GRBs. However, our sample only covers the interval from 10 to 100 photons cm^{-2} s^{-1}. Similarly, our bursts cover just two orders of magnitude although these 1405 GRBs cover six orders of magnitude in the distributions of the energy fluence.

3.2. *Evolution Patterns of* E_p *and* α

In this section, we give the spectral analysis results that include the time-integrated spectral results and the time-resolved spectral results. Table 2 shows the results of the time-integrated spectral fits for all samples. Table 3 shows all pieces of information in the time-resolved spectral analysis. Figure 4 presents a comparison between the histogram of α in the time-integrated spectra in our energy range and the BATSE energy range. Figure 5 shows a comparison between our results and the results of the GBM catalog. Figure 6 shows the spectral evolutions for all of the bursts in our sample. The histograms of E_p and α obtained by performing the detailed time-resolved spectral analysis have been shown in Figure 7.

3.2.1. *The Time-integrated Spectral Results*

The time-integrated spectra reflect the overall emission properties but do not exhibit any spectral evolution. Table 2 shows the results of the time-integrated spectral fits for all samples. Listed in this table are the 36 GRBs in our sample that satisfy our criteria in this study (Col. 1), the redshift of them (Col. 2), the duration interval of T_{90} (Col. 3), the integrated range in our analysis (Col. 4), the low-energy photon index α in the time-integrated analysis (Col. 5), the high-energy photon index β in the time-integrated analysis (Col. 6), the peak energy in the time-integrated analysis (Col. 7), and the reduced χ^2 (Col. 8).

There are 11 GRBs with known redshift. The duration values of T_{90} for most of them in our sample seem to be from 20 to 100 s. As we all know, the typical values of the low-energy photon index α and peak energy E_p are ~ -1.0 and $\sim$300 keV, respectively, for the time-integrated spectra based on statistical studies such as Preece et al. (2000), Kaneko et al. (2006), Zhang et al. (2011), Goldstein et al. (2012), and Geng & Huang (2013). While the typical value of α in our sample is ~ -0.9 obtained from Table 2, which is larger than the statistical study of a large sample of GRBs, the E_p is similar to previous statistics. It is curious that the typical α value for the LLE bright bursts in our sample is different from the BATSE bright bursts (Preece et al. 2000). To explore the possible cause of the discrepancy, we limit the *Fermi* spectral fitting only to the BATSE energy range, but we do not get a similar typical α value to Preece et al. (2000). We found that this typical value would be smaller if we select fewer bursts as the sample in our study. So, we estimate that the two typical α values for LLE bright bursts and BATSE bright bursts would be similar if we have enough bursts in the study. Besides, four time-integrated values of α, in GRB 080825C (~ -0.6197), GRB 130502B (~ -0.6279), GRB 141028A (~ -0.6429), and GRB 180305A (~ -0.3126), violate the synchrotron limit.

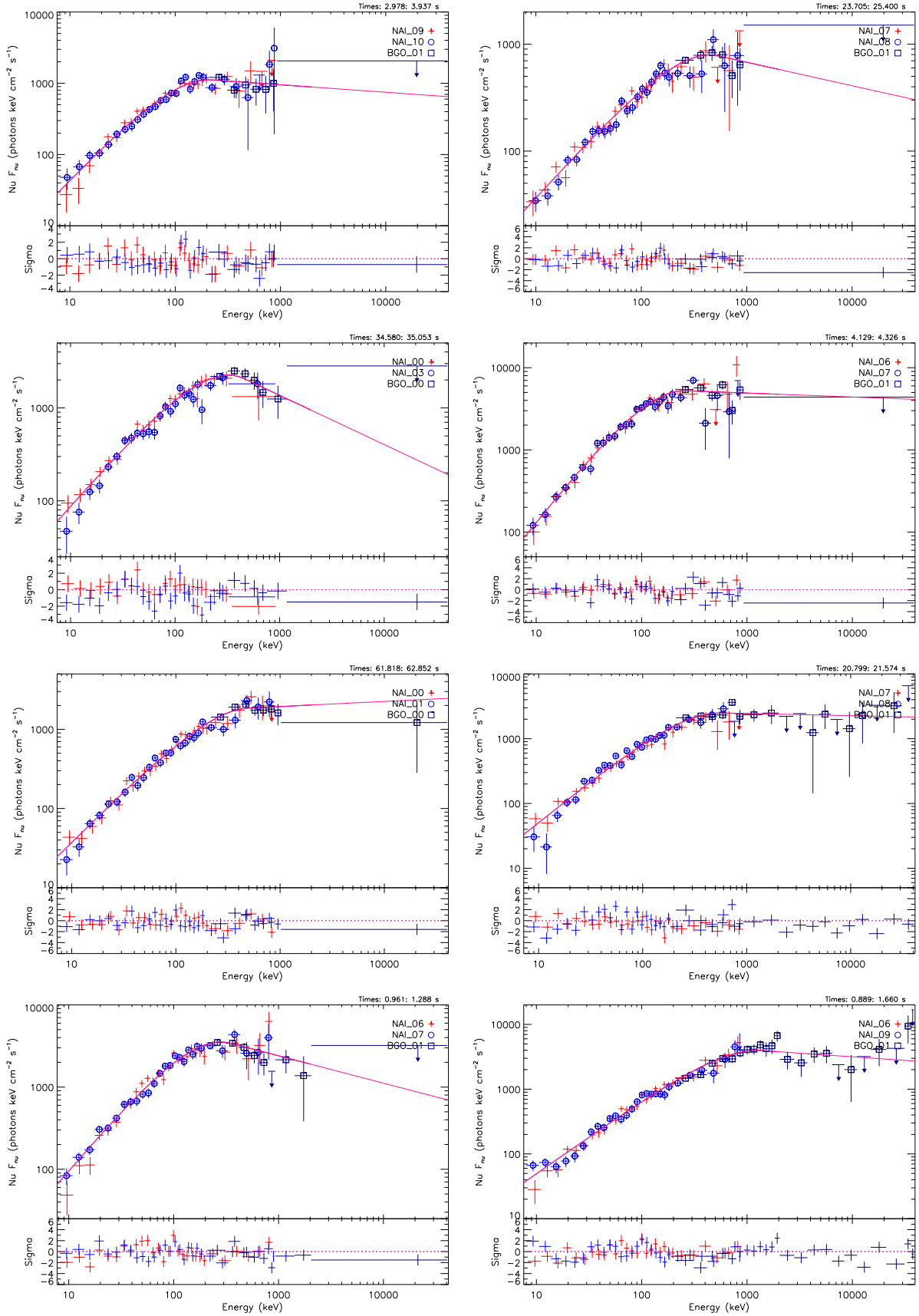

Figure 2. Spectra with the best Band-fitting results around the peak flux for all of the bursts in our sample. The first one is consistent with GRB 080825C, the last is consistent with GRB 180305A. All of them are consistent with the results in Table 1 from GRB 080825C to GRB 180305A.

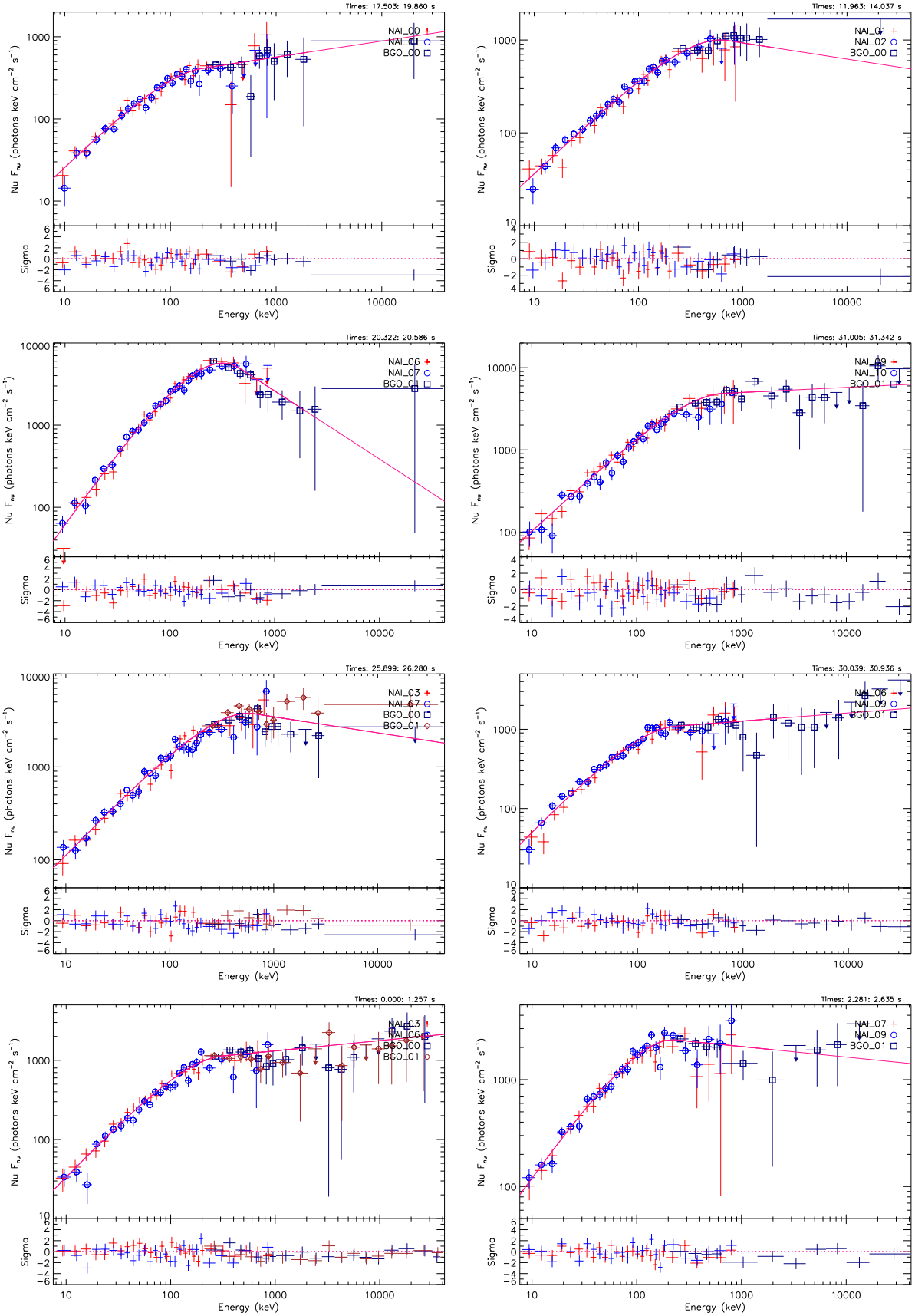

Figure 2. (Continued.)

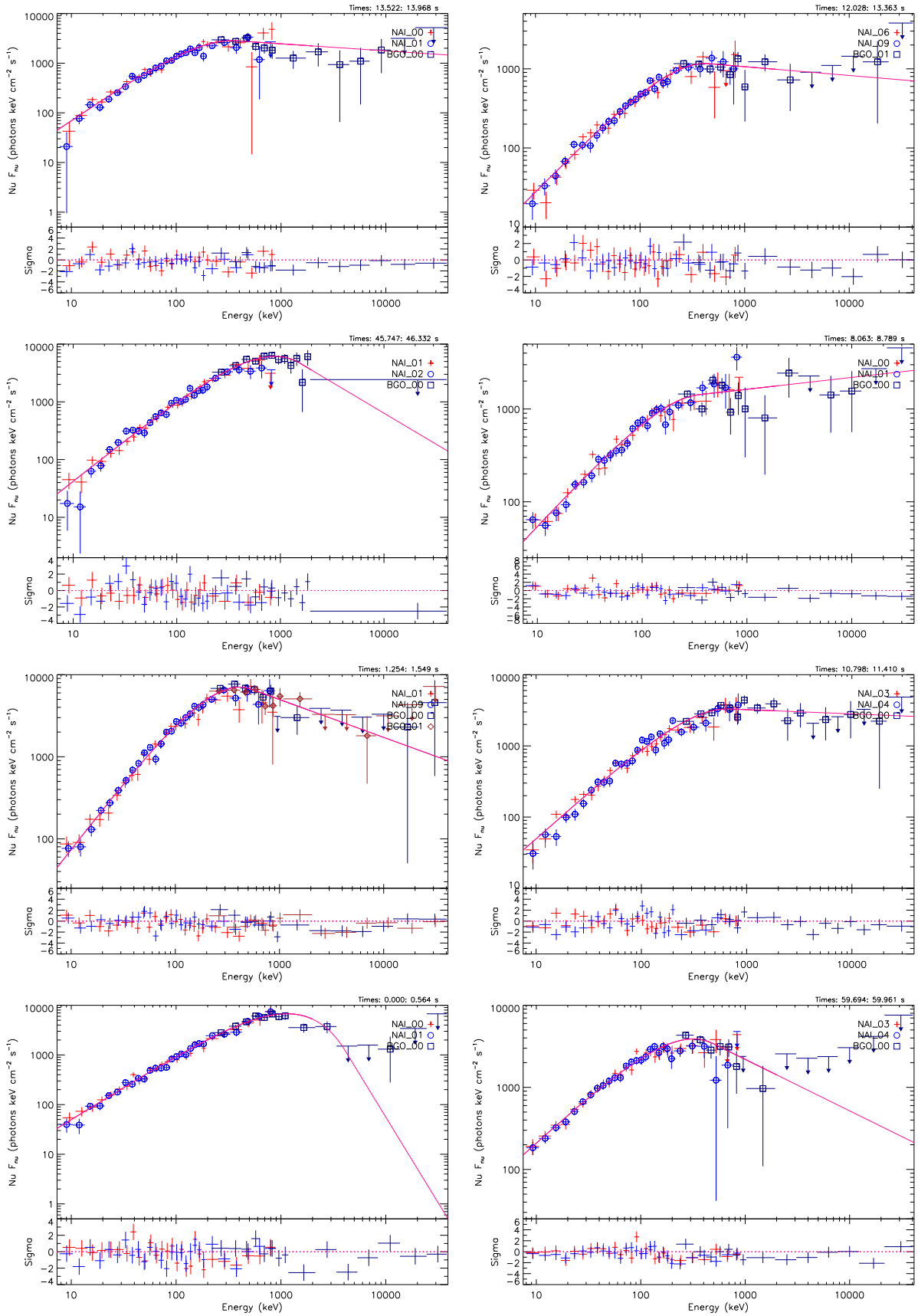

Figure 2. (Continued.)

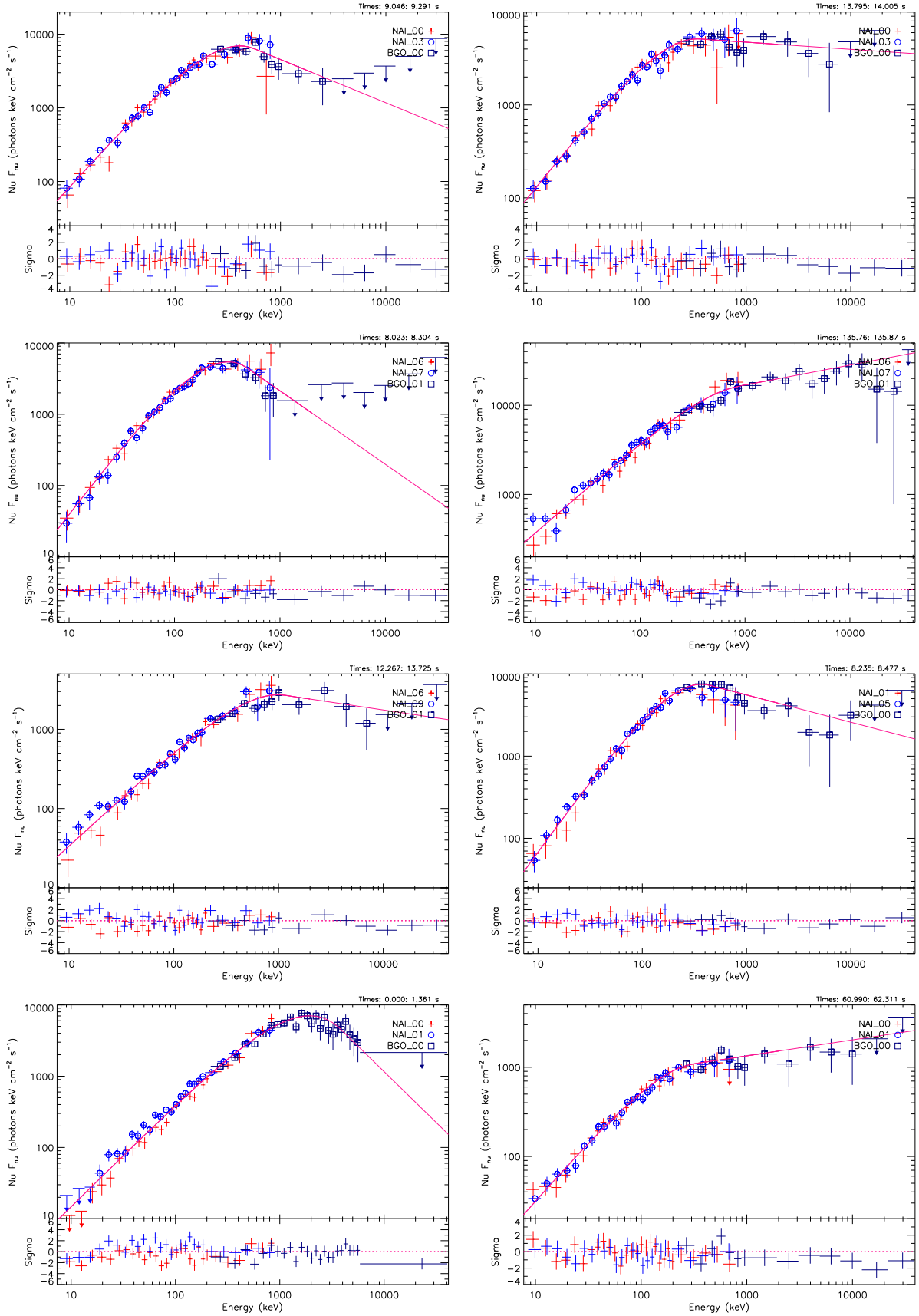

Figure 2. (Continued.)

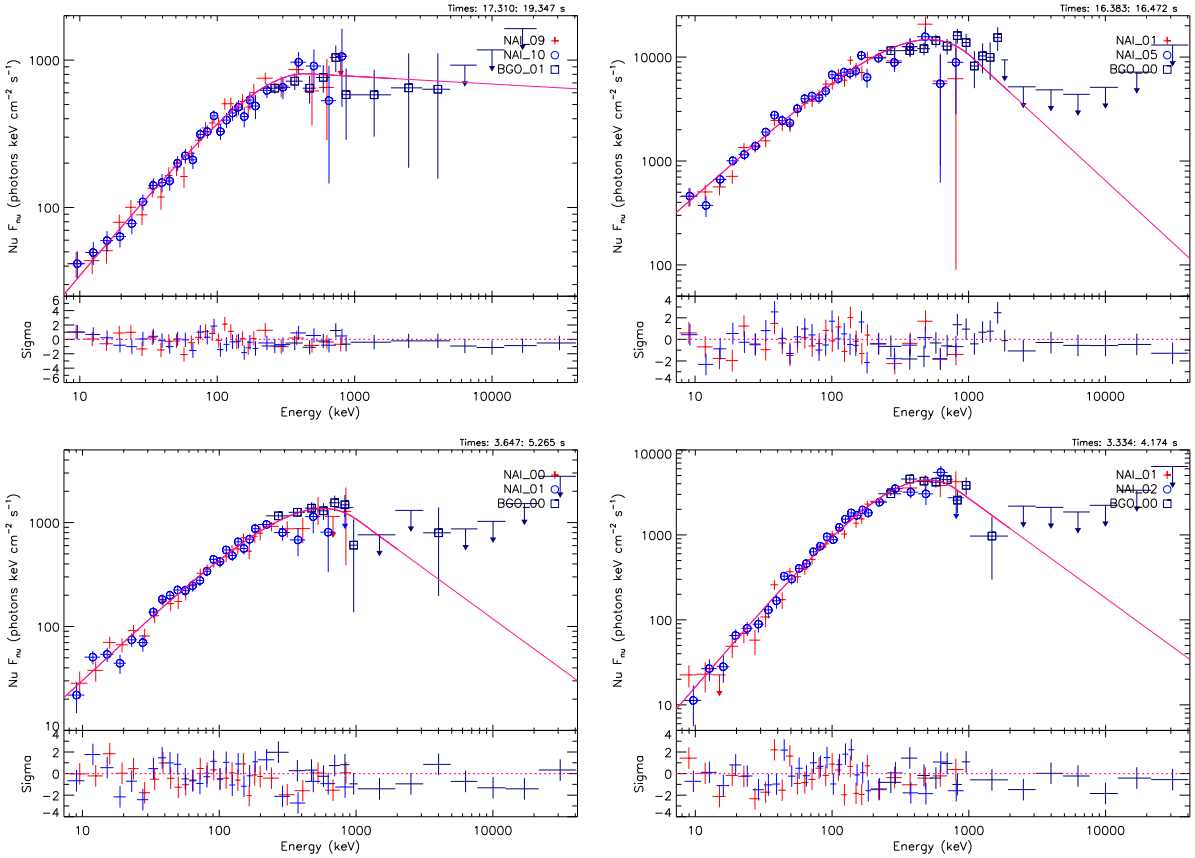

Figure 2. (Continued.)

Similarly, we also compared our results with Gruber et al. (2014). In Figure 5, the distributions of the low-energy spectral indices, high-energy spectral indices, peak energy E_p, energy flux, photon flux, and energy fluence obtained from our time-integrated spectral fits during the whole interval are shown in red dashed–dotted–dotted lines. Meanwhile, the blue short dashed–dotted lines show the corresponding distributions for the BEST-Band sample in Gruber et al. (2014). The energy flux, photon flux, and energy fluence are in the interval from 10 keV to 1 MeV. The overall distribution of α is similar to that found in the BEST-Band sample, for which the typical value is ~ -0.9 for both of them. In the distribution of β, they are different because of their different distribution structures and peaks. However, they are both concentrated in the interval from -2.6 to -1.6, although the β values in our bursts are generally smaller. Ackermann et al. (2012) pointed out that the inclusion of *Fermi*/LAT upper limits in the fitting process can make β steeper. Perhaps the reason why our β values are generally smaller is that the LAT detector observed these bursts. In contrast, the other four parameters, peak energy, energy flux, photon flux, and energy fluence, are generally larger than the BEST-Band bursts. For most of the LLE bursts, the E_p is larger than 150 keV, but it is smaller than 150 keV for most of the BEST-Band sample. We find that 66.7% of the BEST-Band bursts have an energy flux value that is smaller than 1×10^{-6} erg cm^{-2} s^{-1}, while 83.3% of our bursts have a value that is larger than 1×10^{-6} erg cm^{-2} s^{-1}. The two distributions of the photon flux both generally peak around 4–6.5 photon cm^{-2} s^{-1}. Besides, 61.7% of the BEST-Band bursts have a photon flux value that is smaller than 6.5 photon cm^{-2} s^{-1}, while 63.9% of the LLE bursts have a value that is larger than 6.5 photon cm^{-2} s^{-1}. More than half of the BEST-Band bursts have an energy fluence with the value of $<2.5 \times 10^{-5}$ erg cm^{-2}, but all of the LLE bursts have an energy fluence with the value of $>2.5 \times 10^{-5}$ erg cm^{-2} except for GRB 140102A. Meanwhile, 15 GRBs show an energy fluence with the value of $>1 \times 10^{-4}$ erg cm^{-2} for the LLE sample, but only eight GRBs show this value for the BEST-Band sample.

3.2.2. The Time-resolved Spectral Results

We present the results of the time-resolved spectral analysis and the evolution patterns of E_p and α in this section. The fitting results of the parameter correlations and the spectral evolutions of E_p and α have been shown in Table 3. Listed in this table are the 36 GRBs in our sample that satisfy our criteria in this study (Col. 1), the detectors used (Col. 2), the number of the time slice (Col. 3), the Pearson's correlation coefficient r in the E_p–F correlation (Col. 4), the Pearson's correlation coefficient r in the α–F correlation (Col. 5), the Pearson's correlation coefficient r in the E_p–α correlation (Col. 6), the spectral evolution patterns of E_p and α (Col. 7), whether the values of α in the time-resolved spectral analysis are larger than the synchrotron limit ($-\frac{2}{3}$) or not (Col. 8), the Pearson's correlation coefficient r in the α–F correlation obtained from the simulation (Col. 9), and the Pearson's correlation coefficient r in the E_p–α correlation obtained from the simulation (Col. 10). Figure 6 shows the spectral evolutions for all the LLE bursts. The histograms of E_p and α obtained by

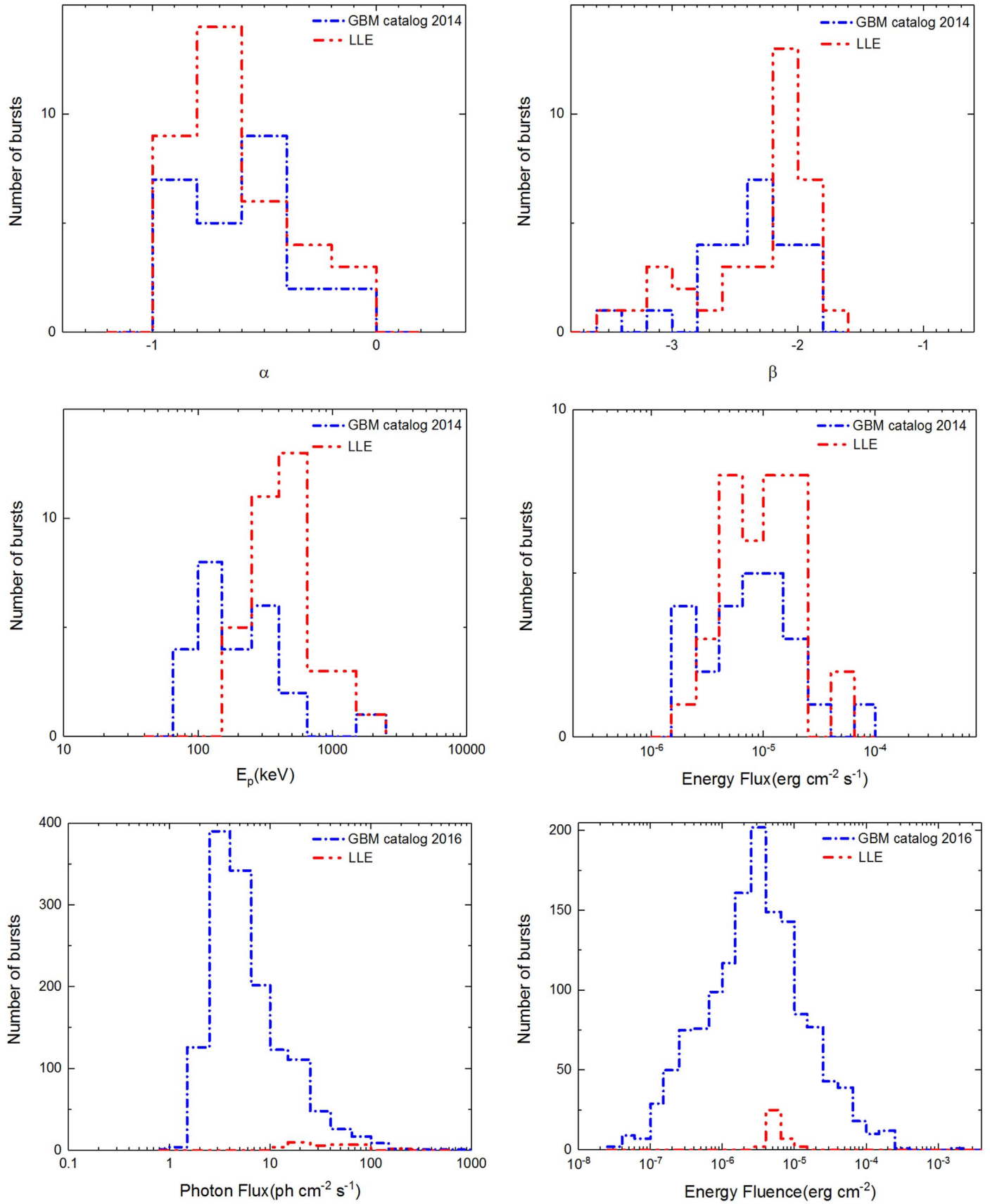

Figure 3. Distributions of the low-energy spectral indices, high-energy spectral indices, peak energy E_p, energy flux, photon flux, and energy fluence obtained from our time-resolved spectral fits around the peak flux (red dashed–dotted–dotted lines). The blue short dashed–dotted lines show the corresponding distributions in Gruber et al. (2014) or Narayana Bhat et al. (2016).

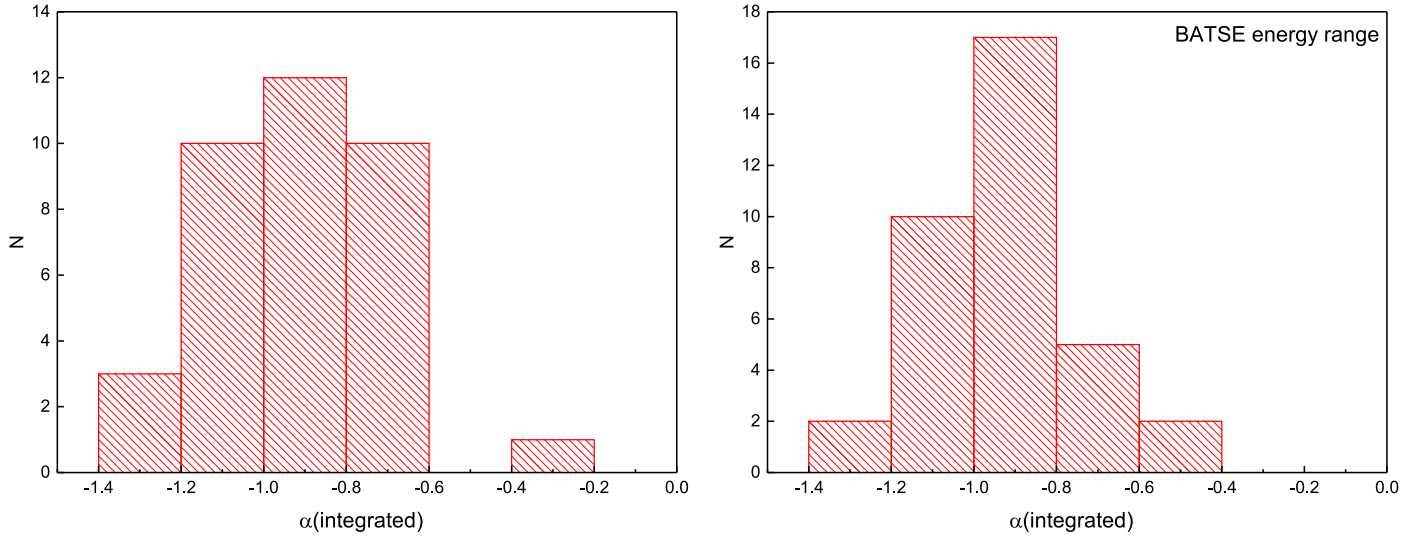

Figure 4. Comparison between the histogram of α in the time-integrated spectra in our energy range and the BATSE energy range. The left panel represents the histogram of α in the time-integrated spectra in the *Fermi*-GBM energy range (from 8 keV to 40 MeV). The right panel shows the BATSE energy range (from 28 to 1800 keV).

performing the detailed time-resolved spectral analysis have been shown in Figure 7.

As described above, there are three types of evolution patterns of peak energy E_p: (i) "hard-to-soft" trend; (ii) "flux-tracking" trend; (iii) "soft-to-hard" trend or chaotic evolutions. A recent study pointed out that the first two patterns are dominant. A good fraction of GRBs follow the "hard-to-soft" trend (about two-thirds), and the rest should be the "flux-tracking" pattern (about one-third). The low-energy photon index α does not show a strong general trend compared with E_p although it also evolves with time instead of remaining constant. All of these results can contribute to the statistical study for the large sample of bursts in the literature. Our study may give birth to different and new progress in the field of *Fermi*-LLE gamma-ray bursts.

We investigate Figure 6 in detail and identify the evolution patterns of E_p and α as six categories. In fact, five groups are enough to depict the evolution pattern of E_p: six GRBs exhibit the "hard-to-soft" pattern; two GRBs undergo the transition from "soft-to-hard" to "hard-to-soft" (GRBs 131108A and 150510A); five GRBs show "intensity-tracking" (compared with flux); for 22 GRBs, a good fraction of those samples exhibit the "rough-tracking" (compared with flux) behavior; the other two GRBs, 150314A and 170510A, exhibit chaotic evolutions. It is noticeable that, GRB 171210A, a special burst, shows the rough "flux-tracking" pattern with the superposition of "hard-to-soft" evolution. It is obvious that the "flux-tracking" pattern is very popular for most of the bursts, the total number including "intensity-tracking" and "rough-tracking" is 27, which means that 75% of these bursts follow the "flux-tracking" pattern. For the evolution of α, it consists of a "hard-to-soft" pattern, "soft-to-hard" to "hard-to-soft" pattern, "intensity-tracking" pattern, "rough-tracking" pattern, "anti-tracking" pattern, "rough-tracking" combined with "hard-to-soft" pattern, and chaotic evolution pattern (all "-tracking" patterns are based on the evolution of energy flux). Three GRBs exhibit the "hard-to-soft" pattern; one GRB undergoes the transition from "soft-to-hard" to "hard-to-soft" (GRB 110721A); two GRBs show an "intensity-tracking" pattern; most of the bursts, 26 GRBs, exhibit "rough-tracking;" three GRBs exhibit the chaotic evolution; the rest (GRBs 150202B and 170115B), exhibit the "anti-tracking" pattern. Similarly, we found that GRB 150510A shows the "rough-tracking" pattern combined with a "hard-to-soft" pattern. All of these evolution patterns have been summarized in Table 3. One can obtain the specific evolution pattern of E_p and α for each burst from this table.

In addition, from Figure 7, which presents the histograms of E_p and α obtained by performing a detailed time-resolved spectral analysis, the typical value is consistent with the statistical study of a large sample in the literature both for E_p ($\sim$300 keV) and α (~-0.8) in all 712 spectra. But such a value of α is inapplicable for some bursts such as GRBs 080825C, 141028A, 170115B, and 180305A; the values of α for all slices are larger than the synchrotron limit ($-\frac{2}{3}$). In particular, GRB 170115B is different from the other three bursts because the value of α (~-0.8) in the time-integrated spectrum is smaller than the synchrotron limit, while the values in all the time-resolved spectra are larger than $-\frac{2}{3}$. However, for the other three bursts, the value of α is larger than the limit both for the time-integrated spectrum and each time-resolved spectrum. On the other hand, its evolution violates most of the bursts, which exhibit "anti-tracking" behavior compared with energy flux, i.e., they are decreasing/increasing when the energy flux is increasing/decreasing. From Table 3, one can also find that only nine GRBs can be classified as the kind for which all of the values of α in the detailed time-resolved spectra do not exceed the synchrotron limit. The values of α for the other 23 GRBs in the detailed time-resolved spectra consist of a fraction that is larger than $-\frac{2}{3}$ and a fraction that does not exceed the synchrotron limit.

3.3. Parameter Correlations

The parameter correlations may play an important role in revealing the nature of the prompt emission for gamma-ray bursts. In this section, the correlations such as E_p–F, α–F, and E_p–α obtained from the time-resolved spectra are shown in Figure 8 for all of the bursts in our sample. The fitting results of the parameter correlations (Pearson's correlation coefficient)

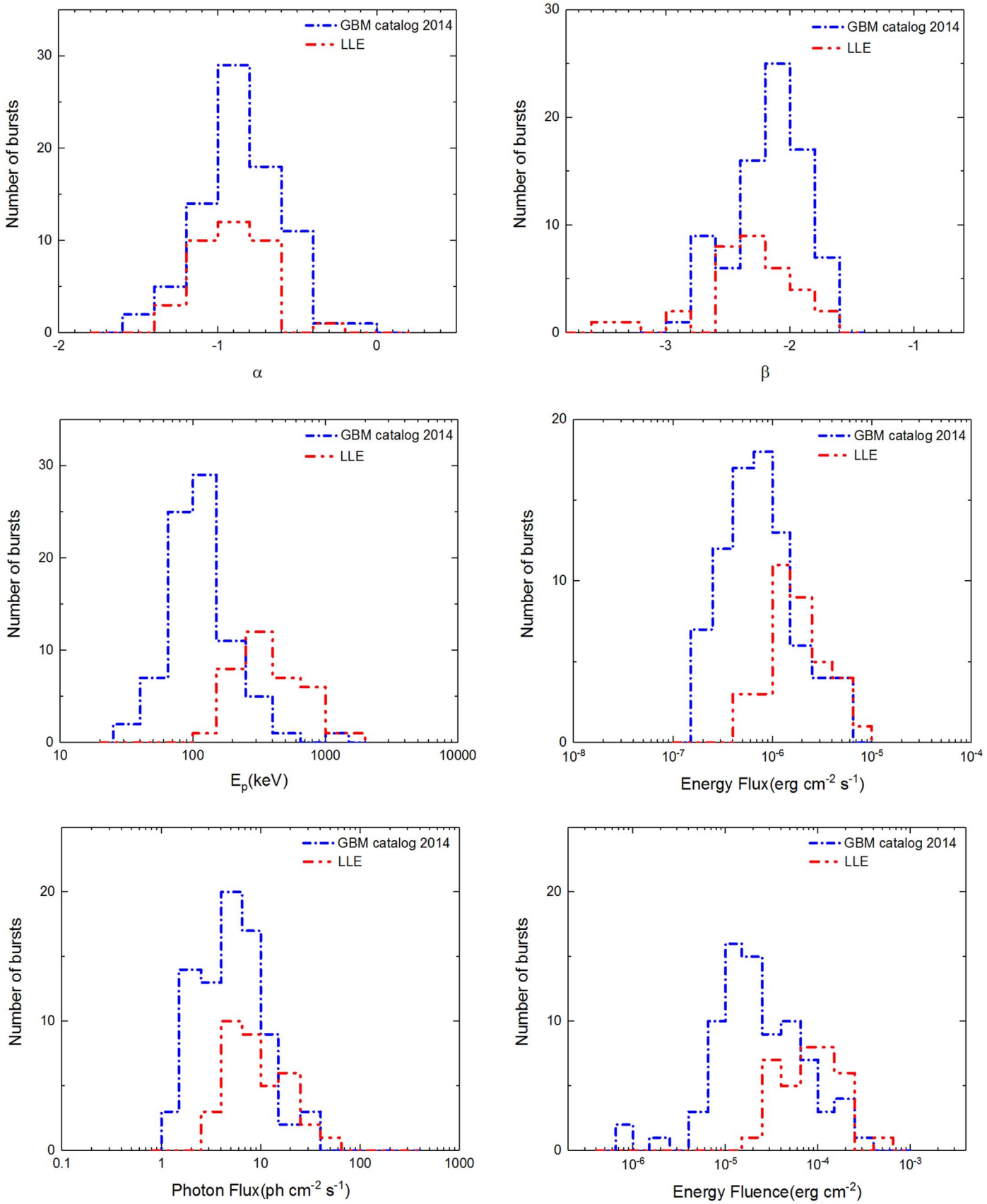

Figure 5. Distributions of the low-energy spectral indices, high-energy spectral indices, peak energy E_p, energy flux, photon flux, and energy fluence obtained from our time-integrated spectral fits (red dashed–dotted–dotted lines). The blue short dashed–dotted lines show the corresponding distributions in Gruber et al. (2014).

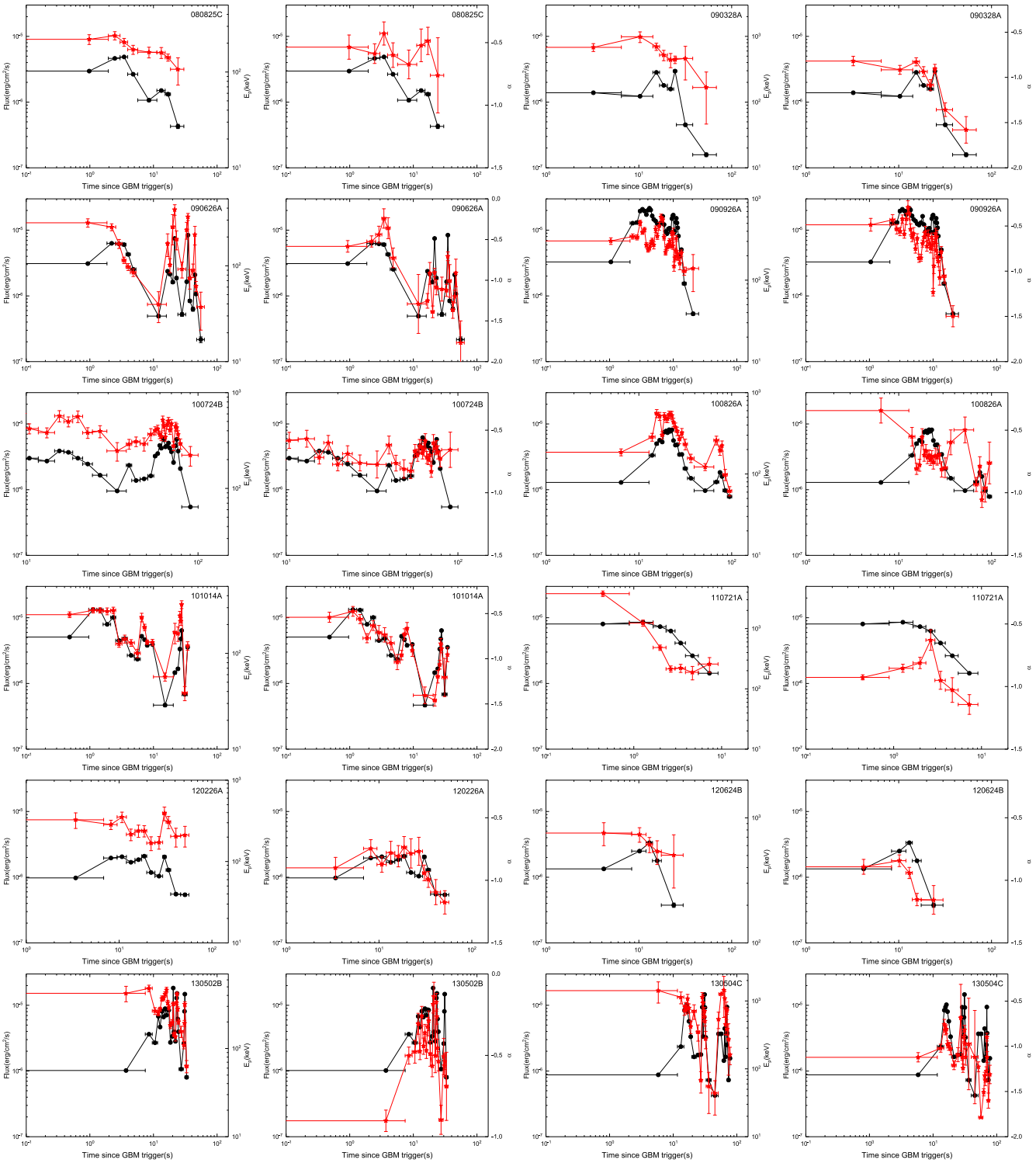

Figure 6. Spectral evolutions. The temporal characteristics of energy flux for all bursts in our sample (the left-hand y-axis), along with time evolutions of E_p and α; both are marked with red stars in the right-hand y-axis.

have been shown in Table 3 (Col. 4, Col. 5, Col. 6) as described in Section 3.2.2. Figure 9 shows the histograms of Pearson's correlation coefficient from the fitting results of parameter correlations such as E_p–F, α–F, and E_p–α.

In our analysis, we investigate Figure 8 in detail, then give the fitting results of the parameter correlations (Pearson's correlation coefficients) in Table 3. Finally, the histograms of Pearson's correlation coefficient from the fitting results of all three parameter correlations are presented in Figure 9. Previous analyses such as Borgonovo & Ryde (2001), Firmani et al. (2009), Ghirlanda et al. (2010), and Yu et al. (2019) have pointed out that the E_p–F relation (Golenetskii et al. 1983), i.e., the relation between the peak energy E_p and energy flux F, exhibits three main types: (i) a non-monotonic relation

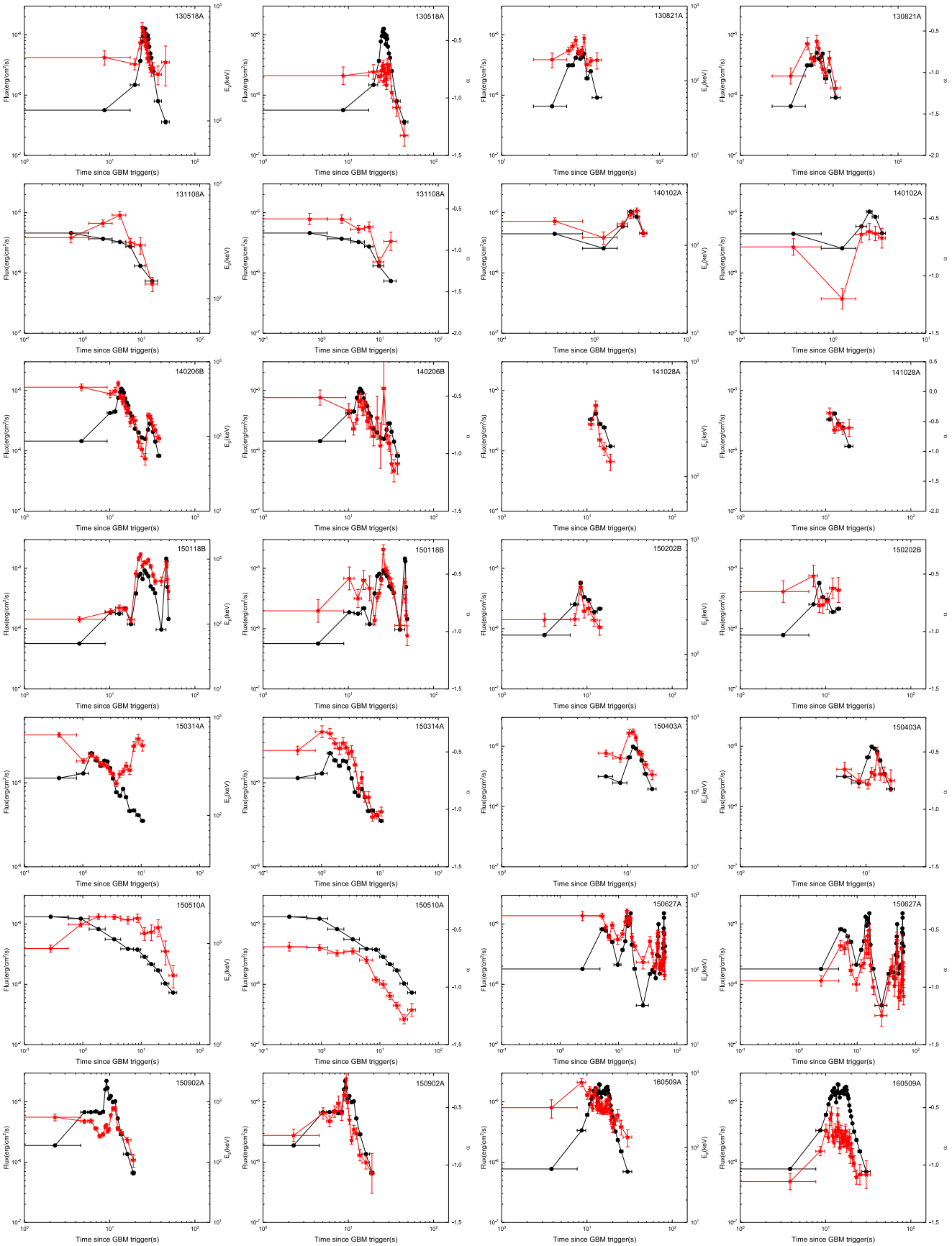

Figure 6. (Continued.)

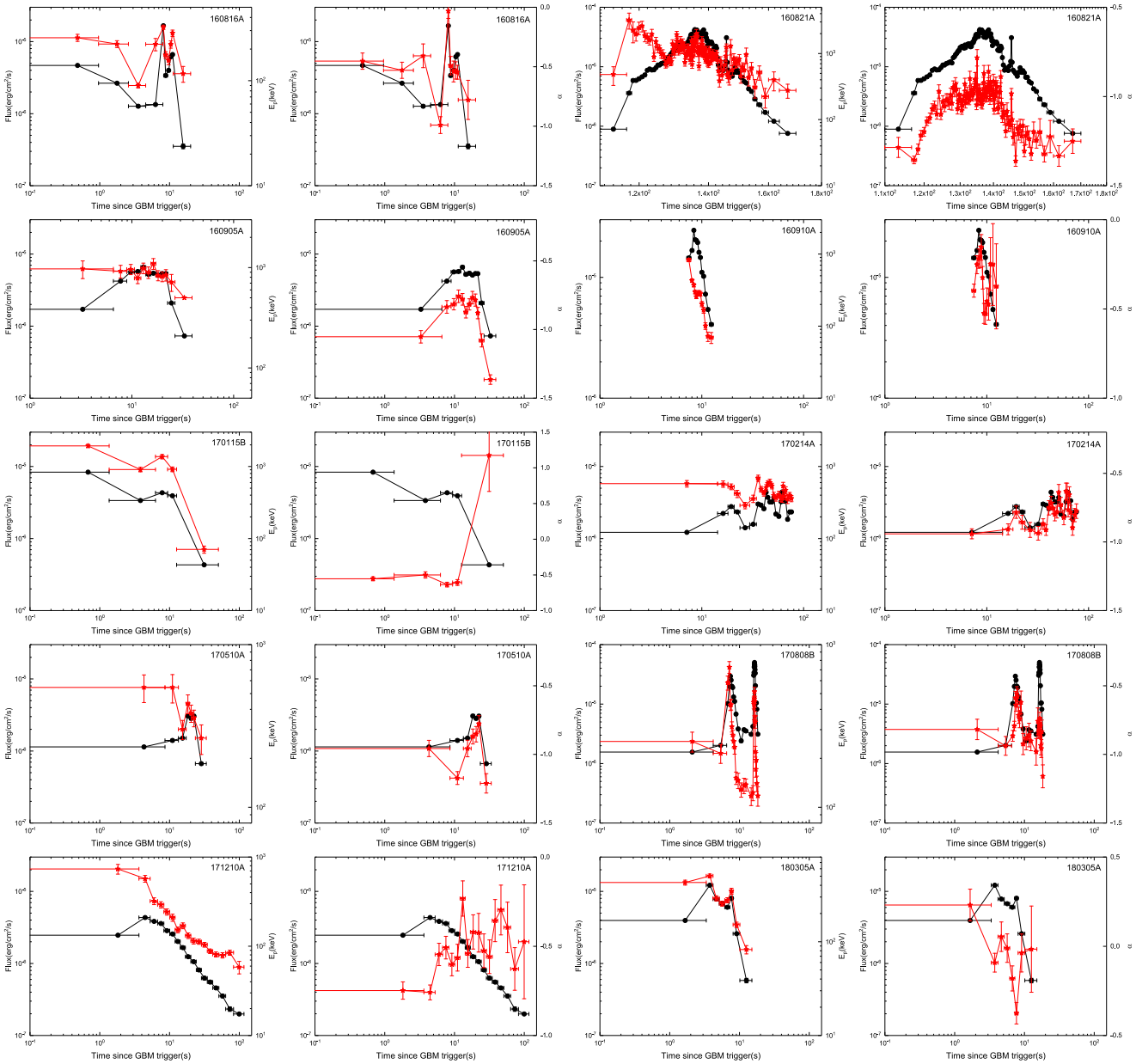

Figure 6. (Continued.)

(containing the positive and negative power-law segments while the break occurs at the peak flux); (ii) a monotonic relation that can be described by a single power law; (iii) no clear trend. For all of our bursts, the most common behavior (in 25 pulses) has a relation described by a single power law, which means that they have a strong positive relation. Of these, 13 GRBs have a very strong positive relation ($r \in$ (0.8, 1.0), see Table 3 and Figure 9) , another 12 GRBs have a strong positive relation ($r \in$ (0.6, 0.8), also see Table 3 and Figure 9). The other 11 GRBs have a positive correlation that is not strong or very strong, but the moderate correlation emerged in eight GRBs , the last three show a weak correlation (GRBs 150314A, 170214A, 170510A). In brief, 69.4% of these bursts show a strong positive correlation and 30.6% of these bursts show a weaker positive correlation compared with the former. However, these results are inconsistent with the study of 38 single pulses in Yu et al. (2019), which shows that 23 single pulses exhibit the non-monotonic relation and 13 pulses exhibit the monotonic relation (the two common behaviors in their study).

Turning to the α–F relation, the study of a large sample of single pulses in Yu et al. (2019) shows a monotonic positive linear relation in the log-linear plots. In the study, the majority of the pulses show a strong positive relation (28 pulses), eight pulses have a very strong positive relation, and only two pulses have a weak correlation. However, the results of our study present at least six types of monotonic linear relation in the log-linear plots. The strong positive correlation is most popular, 23 GRBs show this correlation ($r \in$ (0.6, 1.0)). Of these, 10 GRBs exhibit a very strong positive correlation, which means that the Pearson's correlation coefficient is larger than 0.8. Furthermore, three GRBs show a moderate positive correlation ($r \in$ (0.4, 0.6)). Three GRBs have a weaker positive correlation

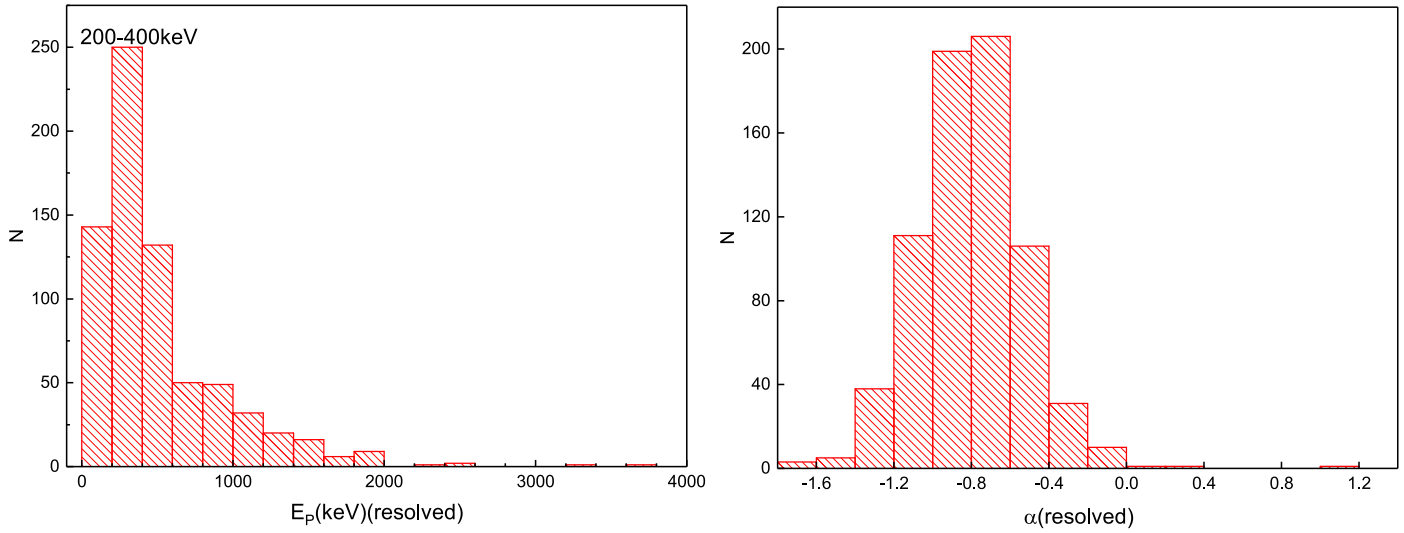

Figure 7. Histograms of E_p and α in a detailed time-resolved spectra. The left panel shows a histogram of E_p, the typical value of E_p is from 200 to 400 keV. The right panel shows a histogram of α, the typical value is ~ -0.8. The typical value is consistent with the statistical study of a large sample in the literature both for E_p and α in all 712 spectra.

($r \in (0.2, 0.4)$). Three GRBs have no correlation between α and F. The other four GRBs differ from them in α–F correlation. In particular, GRB 170115B shows a very strong negative correlation in this relation.

Finally, the E_p–α correlation differs clearly from the first two relations. Only five GRBs have a strong positive relation. Of these bursts, two GRBs have a very strong positive relation, three GRBs have a general strong positive relation. Besides, four GRBs have a moderate positive relation and nine GRBs have a weaker positive relation. Fifteen GRBs have no correlation between E_p and α. Moreover, one can find that two bursts have a strong negative correlation (GRB 150202B, 170115B). In particular, GRB 150202B has a general strong negative correlation while GRB 170115B has a very strong negative correlation with the value of $r = -0.97$. The last one (GRB 171210A) shows a moderate negative correlation.

It is noteworthy that there are two peculiar bursts, GRBs 150202B and 170115B, that have an "anti-tracking" behavior compared with the energy flux for the low-energy photon index α. The negative correlation is exhibited for both their parameter correlations such as α–F and E_p–α correlations. The Pearson's correlation coefficient of α–F is -0.48 for GRB 150202B, which means that it is a moderate negative correlation, and a strong negative correlation ($r = -0.69$) has been shown in E_p–α correlation for this burst. Surprisingly, a very strong negative correlation has been exhibited both for α–F ($r = -0.95$) and E_p–α ($r = -0.97$) correlations for GRB 170115B. Additionally, the value of α in the time-integrated spectrum is smaller than the synchrotron limit, while values of α for all of the slices in the time-resolved spectra that violate the limit for GRB 170115B can be found.

3.4. Whether the Two Observed Strong Positive Correlations are Intrinsic or Artificial

As mentioned in Section 3.3, we found that there are 23 GRBs that show a strong positive correlation in α–F relation in our analysis. Also, five of these 23 GRBs have a strong positive correlation in E_p–α. However, a physical mechanism (either synchrotron or photosphere emission) predicts a low-energy spectral index independent of the flux of the burst. On the other hand, Kaneko et al. (2006) pointed out that a strong anticorrelation was found between the peak energy E_p and low-energy spectral index α both for Band and COMP fits regardless of S/N or the values of other parameters. In consideration of the differences between our results and the previous study, we performed a simulation to identify whether the two observed strong positive correlations are intrinsic or artificial.

We performed the simulation analysis with the RMFIT package as a tool. We take the 23 GRBs that exhibit a strong positive correlation in α–F relation (five GRBs also show a strong positive correlation in E_p–α relation among them) as a template to perform the simulations. The simulation procedure is as follows:

1. Extract the TTE data of the two brightest Na I and the corresponding BGO detectors of those GRBs (23 GRBs, see Figures 10 and 11). We use the Band model with fixed input values of E_p, α, β, and the normalization of the spectrum from the best Band-fitting parameters in the time-integrated spectrum for each burst to produce an intrinsic spectrum.
2. Import the extracted data into RMFIT.
3. Perform a time-resolved spectral fitting analysis in a different flux level (we changed the S/N from 2 to 200, we used values decreased by a step of a factor of 10 until the S/N was 2), and output the fitted parameters.

Similarly, we show the two correlations α–F and E_p–α derived from the simulations in Figures 10 and 11. In our simulations, only 1 GRB, GRB 160905A, shows a strong positive correlation ($r = 0.65$) in α–F correlation. We found that 21 GRBs show a strong anticorrelation except for two GRBs (GRBs 101014A, 131108A) in E_p–α correlation. Comparing the simulated results with the observed results (our fitting results), we think that the two observed strong positive correlations are artificial in our sample except for GRB 160905A in its α–F correlation.

As described in Lloyd-Ronning & Petrosian (2002), a positive correlation between E_p and α is expected due to the instrumental effect, even though the negative correlation is

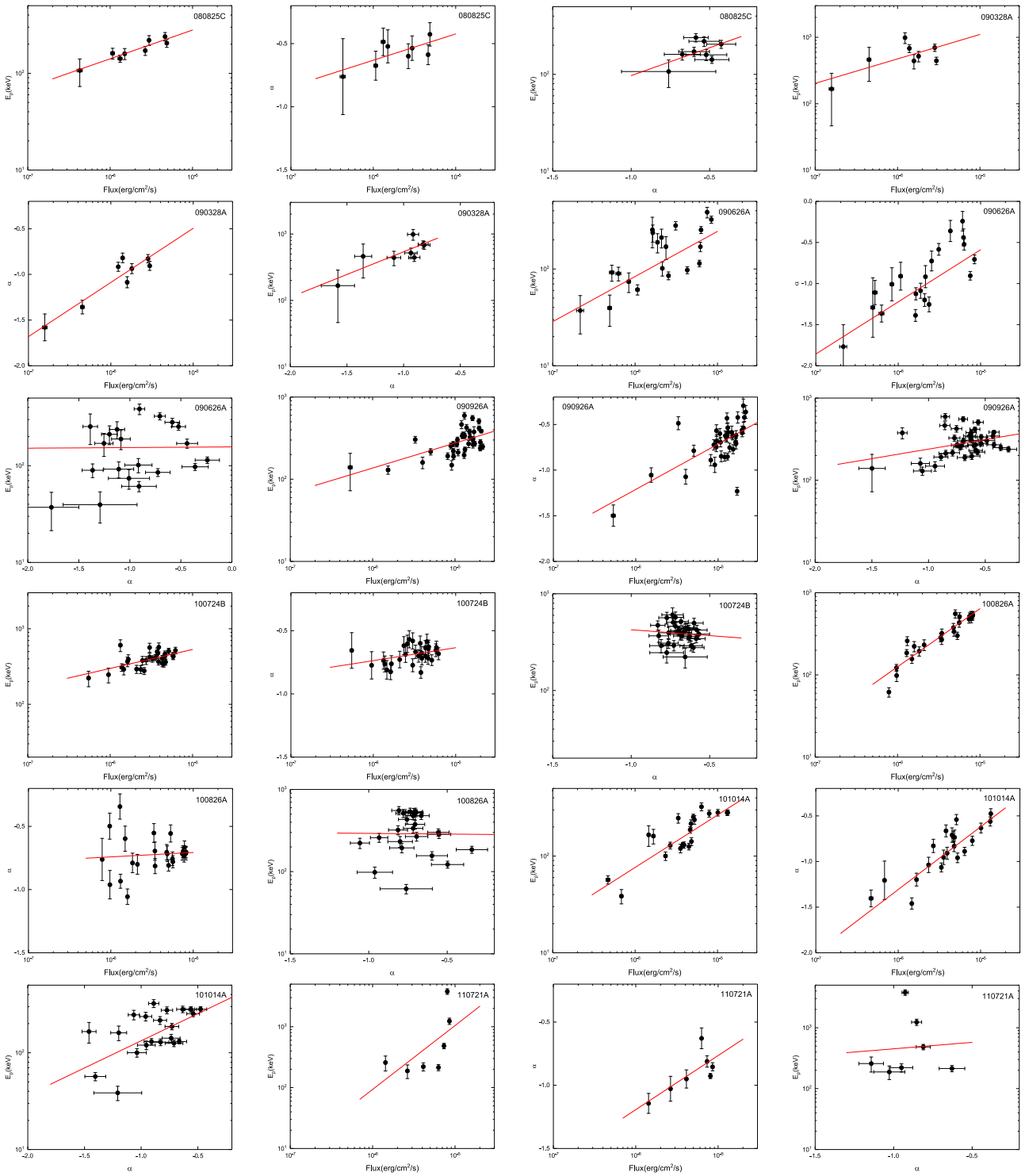

Figure 8. Parameter correlations. The correlations such as E_p–F, α–F, and E_p–α obtained from the time-resolved spectra are shown for all of the bursts in our sample. The red solid line represents the best-linear-fitting result for each burst.

expected in the theory of gamma-ray bursts. If E_p is close to the instrument's lower energy sensitivity limit, the low-energy spectral index α has not yet reached its asymptotic value, and α is softer than its true value. In addition, because the spectrum with a low peak energy will exhibit most of its curvature near the low-energy edge of the instrument, smaller E_p values will increase the uncertainty in the measurement of α. Thus, we will observe the positive E_p–α correlation instead of the expected negative correlation in gamma-ray bursts. Combined with the "flux-tracking" pattern of E_p, on the other hand, it is naturally understandable that the positive α–F correlation will be seen in the observation.

4. Conclusion and Discussion

In this work, after performing a detailed time-resolved spectral analysis of the bright gamma-ray bursts with the detection of *Fermi*-LLE in the prompt phase, we presented all

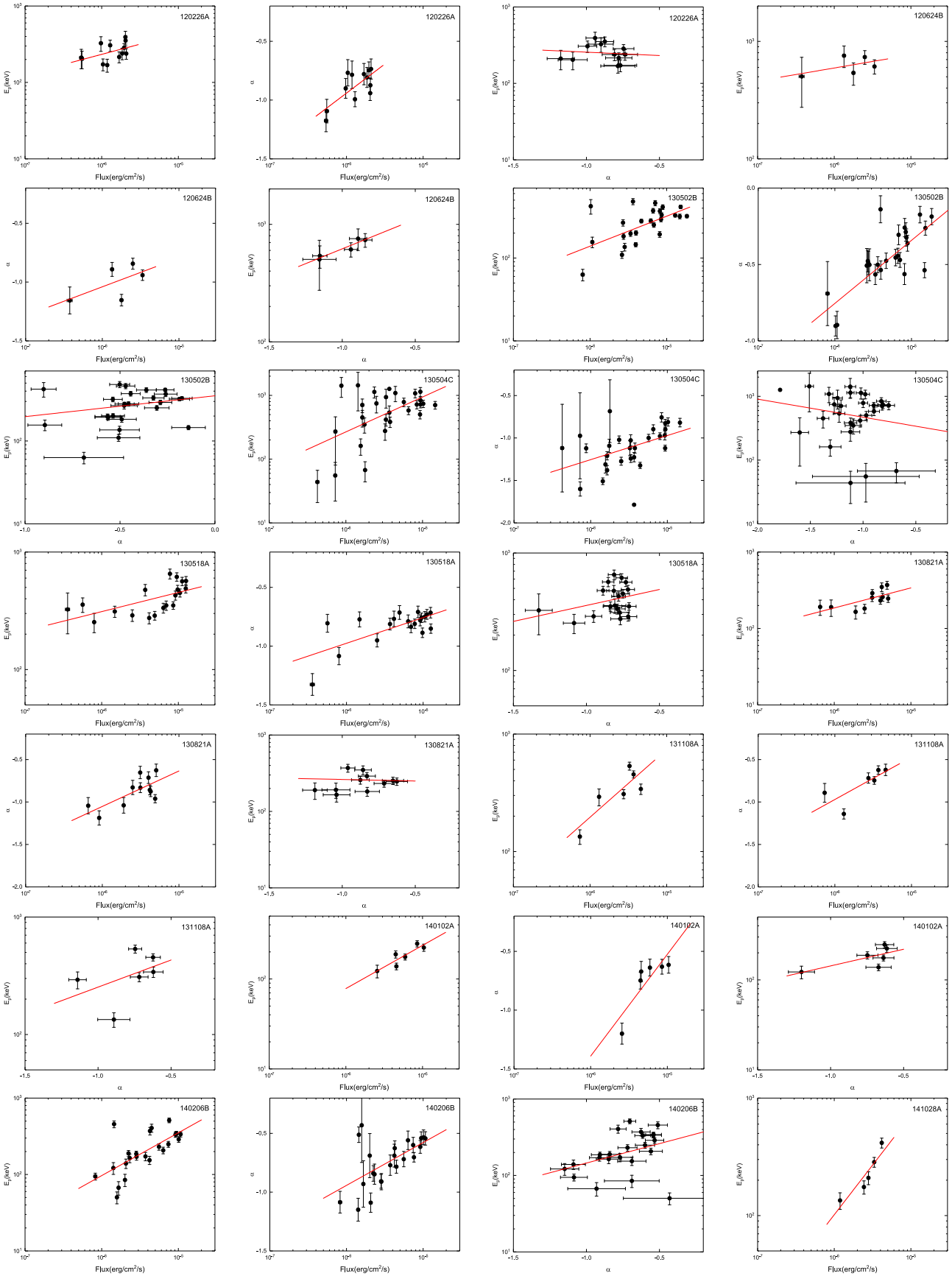

Figure 8. (Continued.)

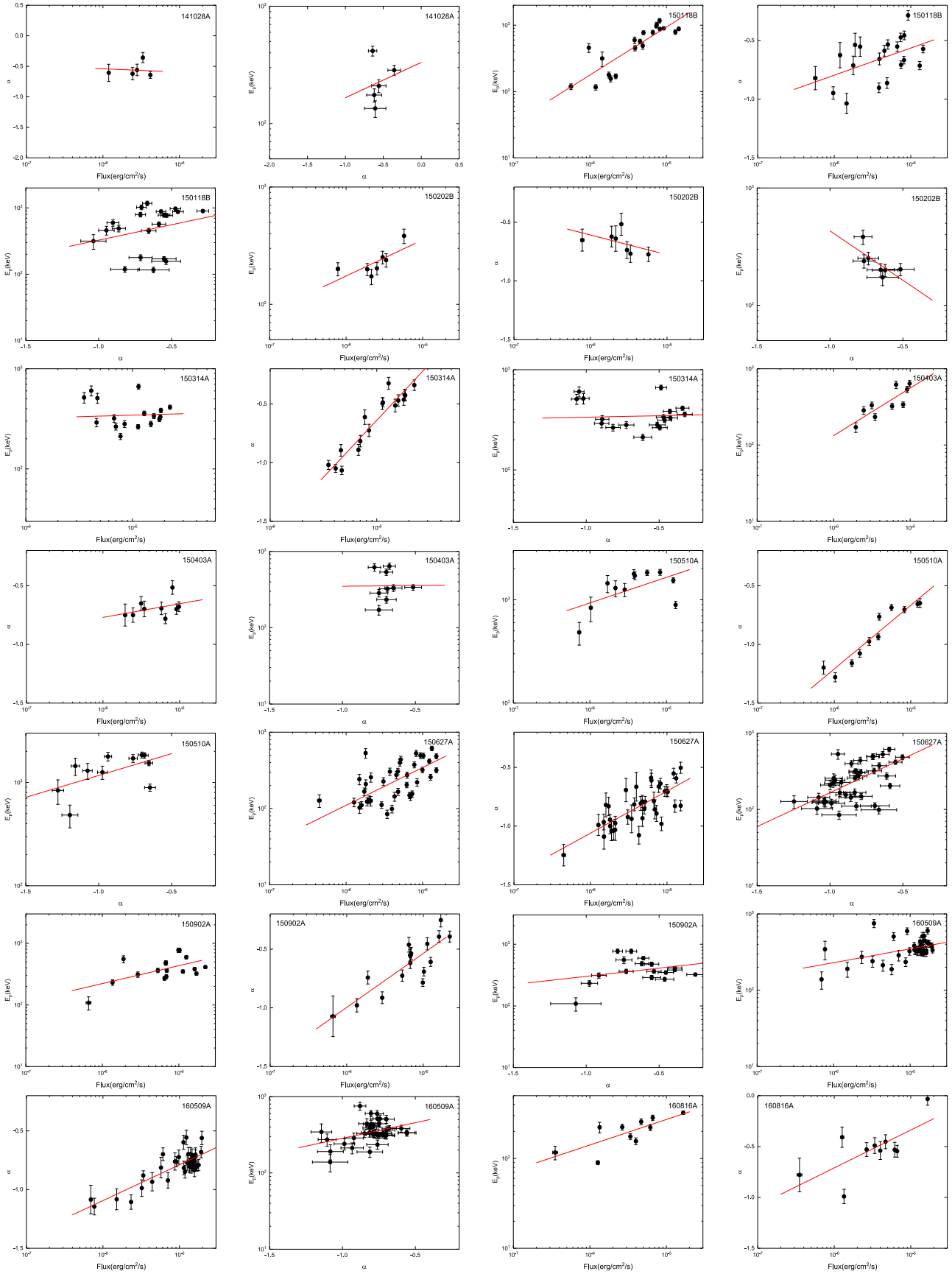

Figure 8. (Continued.)

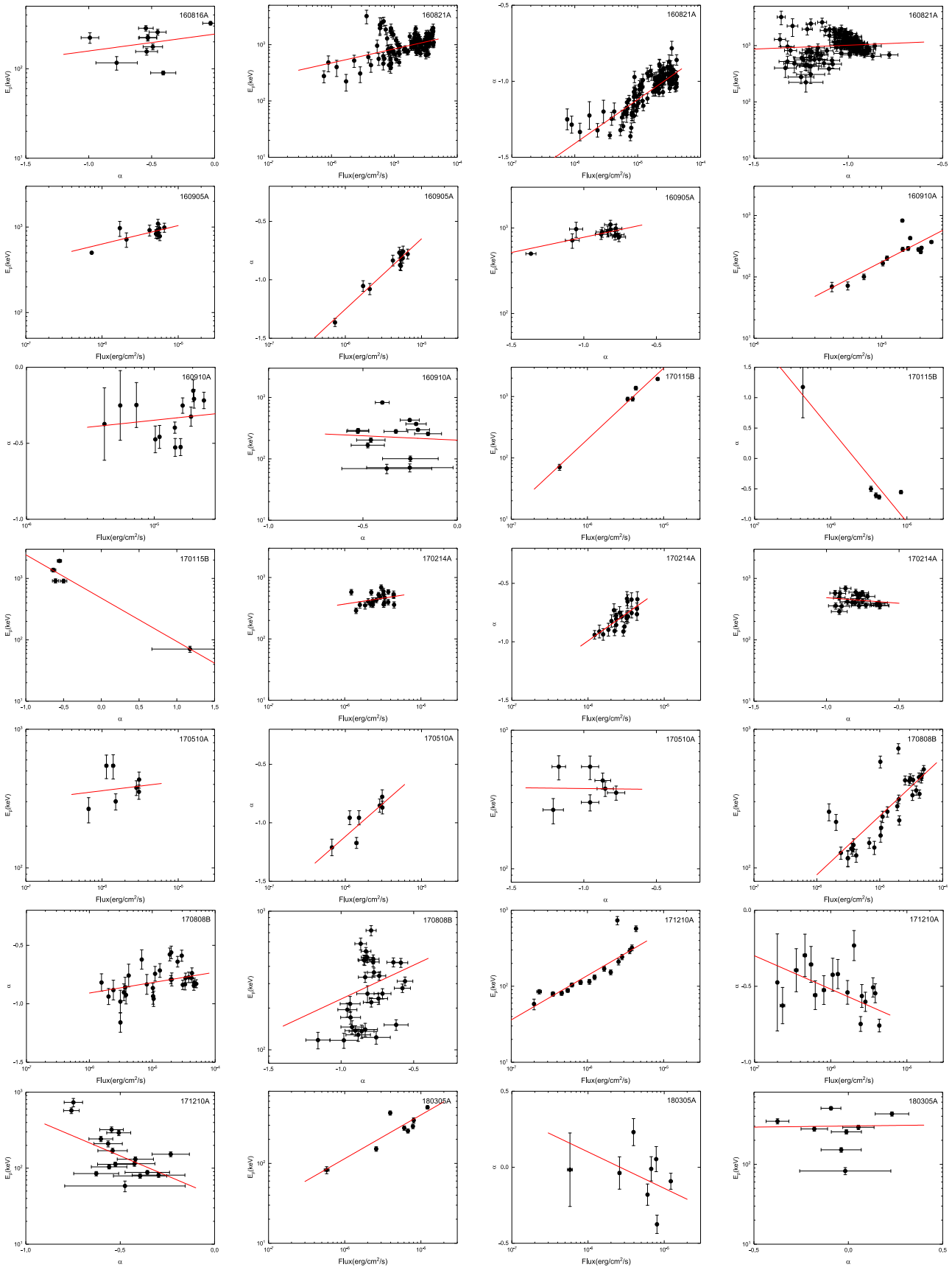

Figure 8. (Continued.)

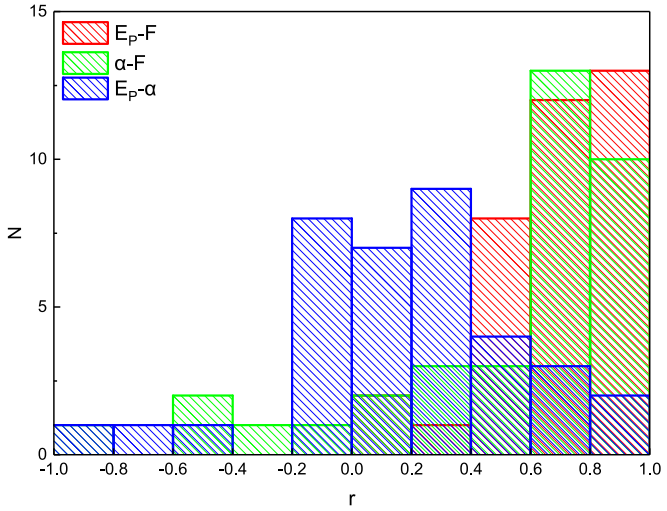

Figure 9. Histograms of Pearson's correlation coefficient from the fitting results of parameter correlations such as E_p–F, α–F, and E_p–α. There is a strong monotonous positive correlation both for E_p–F and α–F correlations in most of our bursts.

the spectra with the best Band-fitting results at peak flux for our bursts. To confirm whether our results are consistent with the *Fermi* team's results, we compared our results with the *Fermi* GRB spectral catalog. Then we gave the evolution patterns of the peak energy E_p and low-energy spectral index α. Also, the statistical analysis for whether the low-energy power-law indices α exceed the synchrotron limit were given. Finally, the parameter correlations such as E_p–F, α–F, and E_p–α were also presented in the analysis. To address whether the two observed correlations α–F and E_p–α are intrinsic or artificial, we performed a simulation.

Meanwhile, some interesting phenomena were found in our *Fermi*-LLE bursts, such as:

1. A single Band function is enough to perform the spectral fitting for every burst around their peak flux.
2. 77.8% of the bursts have an $\alpha_{\max}$, which is larger than the synchrotron limit ($-\frac{2}{3}$) in our bursts.
3. As we all know, the typical value of the low-energy photon index α is ~ -1.0 for the time-integrated spectrum, while the typical value of α in our sample is ~ -0.9.
4. A good fraction of GRBs follow the "hard-to-soft" trend (about two-thirds), and the rest should be the "flux-tracking" pattern (about one-third) in the literature for E_p evolution. However, it is obvious that the "flux-tracking" pattern is very popular for most of the bursts in our study including "intensity-tracking" (five GRBs) and "rough-tracking" (22 GRBs). The total number is 27, which means that 75% of the bursts exhibit the "flux-tracking" pattern. Additionally, the low-energy photon index α does not show a strong general trend compared with E_p although it also evolves with time instead of remaining constant as seen in the literature. We find that 28 GRBs exhibit a "flux-tracking" pattern, which includes "intensity-tracking" (two GRBs) and "rough-tracking" (26 GRBs) in our study. In brief, 77.8% of our bursts exhibit the "flux-tracking" pattern.
5. For the parameter correlations, from Section 3.3, a majority of bursts exhibit a strong (very strong) positive correlation (69.4%) between E_p and F (energy flux). We find that 63.9% of our bursts have a strong (very strong) positive correlation between α and F. But there is no clear behavior in the E_p–α correlation in our sample. Finally, it is noteworthy that a very strong negative correlation has been exhibited both for α–F and E_p–α correlations for GRB 170115B.
6. The two observed strong positive correlations (α–F and E_p–α) are artificial in our sample except for GRB 160905A in its α–F correlation.

Over the last fifty years, research in the field of gamma-ray bursts has made a lot of progress, but there are still some open questions (e.g., Zhang 2011, 2018; Dai et al. 2017; Pe'er 2019). One of the questions is about the radiation mechanism in the prompt emission, that debates whether the GRB prompt emission is produced by the synchrotron radiation or the emission from the photosphere (Vereshchagin 2014; Pe'Er & Ryde 2017; Oganesyan et al. 2018, 2019; Ravasio 2019). However, a unified model has not been provided even though the physical models such as the synchrotron model (Zhang et al. 2016) and subphotospheric dissipation model (Ahlgren et al. 2019) have been used to make the spectral fitting.

As we all know, the Band component in most observed gamma-ray burst spectra seems to be thought of as synchrotron in origin. Two possible cases should be considered; the first one is for the internal shock model (Paczynski & Xu 1994; Rees & Meszaros 1994), which invokes a small radius. The second case invokes a large internal magnetic dissipation radius, the so-called Internal-Collision-induced MAgnetic Reconnection and Turbulence (ICMART) model (Zhang & Yan 2011). For the internal shock model, the peak energy $E_p \propto L^{1/2}\gamma_{e,ch}^2 R^{-1}(1+z)^{-1}$ can be derived from the synchrotron model in Zhang & Mészáros (2002), where L is the "wind" luminosity of the ejecta, $\gamma_{e,ch}$ is the typical electron Lorentz factor of the emission region, R is the emission radius, and z is the redshift of the burst. Then, the tracking behavior will emerge because of the natural relation of $E_p \propto L^{1/2}$. A hard-to-soft evolution pattern of peak energy E_p is predicted for the ICMART model (Zhang & Yan 2011; Uhm & Zhang 2014). On the other hand, Uhm et al. (2018) also pointed out that the "flux-tracking" behavior could be reproduced within the ICMART model if other factors such as bulk acceleration are taken into account. Furthermore, Zhang et al. (2016) demonstrated that the synchrotron model can reproduce the E_p-tracking pattern through the data analysis for GRB 130606B. Therefore, the "flux-tracking" behavior of E_p can be made with both of these two synchrotron models. In short, a hard-to-soft pattern and tracking behavior of E_p can be reproduced successfully in the synchrotron model.

Meanwhile, the photosphere model can also produce an E_p-tracking pattern and a hard-to-soft pattern of E_p successfully (Deng & Zhang 2014; Meng et al. 2019), but this model predicts a hard-to-soft pattern of α instead of α-tracking behavior. It is difficult to produce the observed α-tracking behavior in this model. On one hand, the predicted α value ($\alpha \sim +0.4$) is much harder than that observed (Deng & Zhang 2014). The introduction of a special jet structure is necessary to reproduce a typical $\alpha \sim -1$ (Lundman et al. 2013). On the other hand, this model invokes an even smaller emission radius than the internal shock model, so, the contrived conditions from the central engine are needed to reproduce the tracking pattern of α. However, few bursts exhibit a

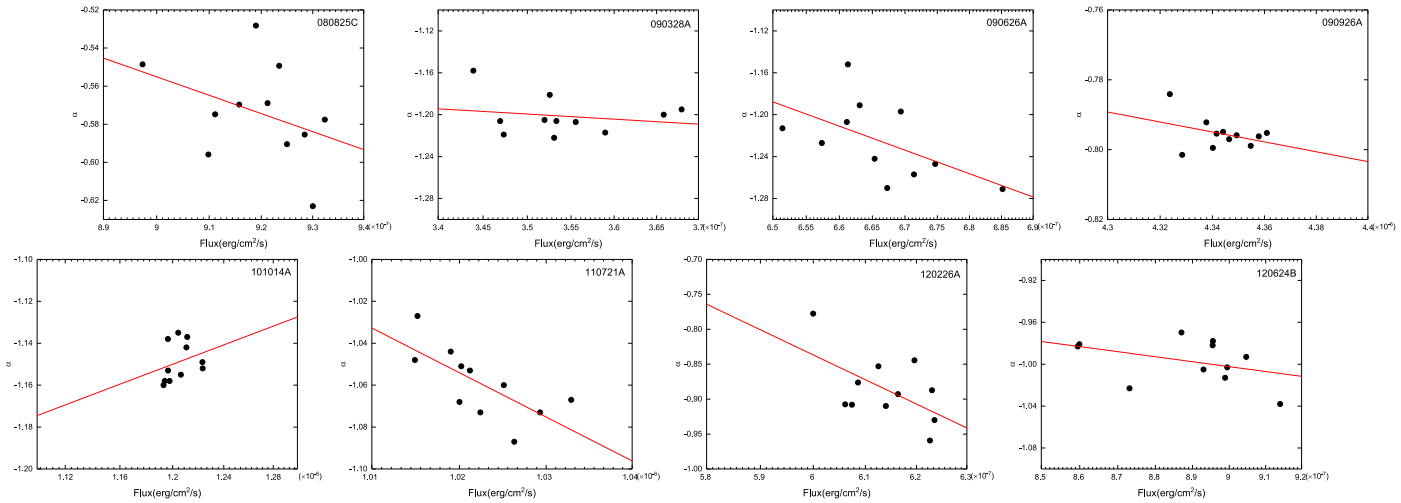

Figure 10. The α–F correlation from the simulation for 23 GRBs, which exhibit a strong positive correlation in α–F correlation. The red solid line represents the best-linear-fitting result for each burst.

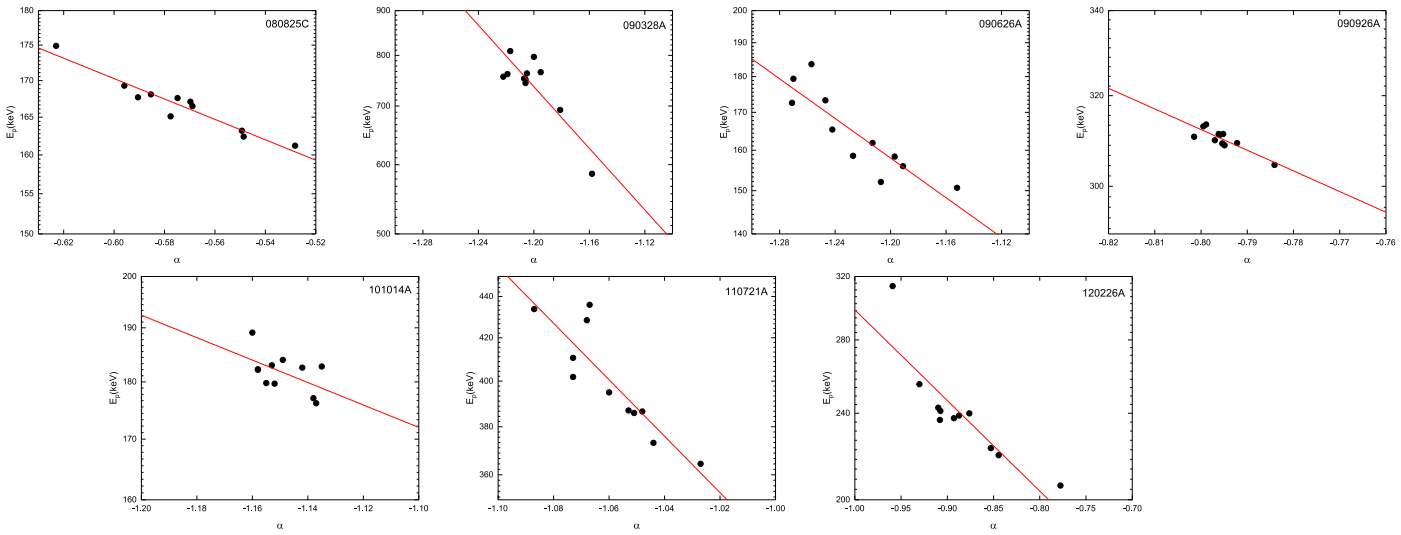

Figure 11. The E_p–α correlation from the simulation for 23 GRBs, which exhibit a strong positive correlation in α–F correlation. The red solid line represents the best-linear-fitting result for each burst.

hard-to-soft pattern in our sample. Besides, Ahlgren et al. (2019) used the physical subphotospheric model to fit the *Fermi* data (including six LLE bursts in our sample; GRBs 090926A, 130518A, 141028A, 150314A, 150403A, 160509A), only 171 out of 634 spectra are accepted (17 out of 135 spectra for the six LLE bursts). As a result, we infer that the great majority of bursts in our sample are dominated by the synchrotron component even though the photosphere component is still not excluded in their prompt phases.

Additionally, the patterns of the peak energy E_p evolution have close connections to the spectral lags (Uhm et al. 2018). In general, the light curves at higher energies peak earlier than those at lower energies, named positive spectral lags. In contrast, for the negative spectral lags, the higher energy emission slightly lags behind the lower energy emission (Uhm & Zhang 2016). Earlier studies in the literature show that only small fraction bursts show negative lags or no spectral lags (Norris et al. 1996, 2000; Liang et al. 2006; Ukwatta et al. 2012). Uhm et al. (2018) studied and provided the connections between the patterns of the E_p evolution and the types of spectral lags (positive or negative lags). According to Uhm et al. (2018), the positive spectral lags can occur if the peak energy exhibits a hard-to-soft evolution pattern, but the negative type cannot occur. When the E_p presents a flux-tracking behavior, both the positive and the negative types of spectral lags can occur. The clue to differentiate between the positive lags and the negative lags for the E_p-tracking pattern comes from the peak location of the flux curve. The peak location of the flux curve slightly lags behind the peak of E_p curve for the former, whereas there is no longer a visible lag between them for the latter (Uhm et al. 2018). Assuming that those bursts that exhibit a hard-to-soft pattern or flux-tracking pattern of peak energy E_p occur as spectral lags, then the positive type of spectral lags will occur at the six bursts that exhibit a hard-to-soft behavior of E_p (GRBs 080825C, 090328A, 110721A, 120624B, 160910A, 171210A). The positive type of spectral lags will also occur at the 12 GRBs because of their peak location of flux curves slightly lags behind their peak of E_p curves (GRBs 090926A, 100826A, 130502B, 130504C, 130518A, 140206B, 150118B, 150627A,

160509A, 160821A, 170214A, 170808B). The negative lags will occur at the rest of the bursts because there is no visible lag between the two peaks (GRBs 090626A, 100724B, 101014A, 120226A, 130821A, 140102A, 141028A, 150202B, 150403A, 160816A, 160905A, 170115B, 180305A).

We thank the anonymous referee for helpful suggestions. We also thank Lei-Ming Du, Zhao-Yang Peng, and Dao-Zhou Wang for their help. We acknowledge the use of the public data from the Fermi data archives. This work is supported by the National Natural Science Foundation of China (grant Nos. 11673006, U1938201, and 11533003), the Guangxi Science Foundation (grant Nos. 2016GXNSFFA380006, 2017AD22006, 2017GXNSFBA198206, and 2018GXNSFGA281007), the One-Hundred-Talents Program of Guangxi colleges, and High level innovation team and outstanding scholar program in Guangxi colleges.

ORCID iDs

Ming-Ya Duan https://orcid.org/0000-0001-5487-4537
Xiang-Gao Wang https://orcid.org/0000-0001-8411-8011

References

Ackermann, M., Ajello, M., Baldini, L., et al. 2012, ApJ, 754, 121
Acuner, Z., & Ryde, F. 2018, MNRAS, 475, 1708
Ahlgren, B., Larsson, J., Ahlberg, E., et al. 2019, MNRAS, 485, 474
Ajello, M., Arimoto, M., Axelsson, et al. 2019, ApJ, 878, 52
Atwood, W. B., Abdo, A. A., Ackermann, M., et al. 2009, ApJ, 697, 1071
Axelsson, M., Baldini, L., Barbiellini, G., et al. 2012, ApJL, 757, L31
Band, D., Matteson, J., Ford, L., et al. 1993, ApJ, 413, 281
Band, D. L. 1997, ApJ, 486, 928
Bhat, P. N., Fishman, G. J., Meegan, C. A., et al. 1994, ApJ, 426, 604
Borgonovo, L., & Ryde, F. 2001, ApJ, 548, 770
Burgess, J. M., Bégué, D., Greiner, J., et al. 2019, NatAs, 4, 174
Burgess, J. M., Preece, R. D., Connaughton, V., et al. 2014, ApJ, 784, 17
Colgate, S. A. 1974, ApJ, 187, 333
Crider, A., Liang, E. P., Smith, I. A., et al. 1997, ApJL, 479, L39
Dai, Z., Daigne, F., & Mészáros, P. 2017, SSRv, 212, 409
Deng, Wei, & Zhang, Bing 2014, ApJ, 785, 112
Duan, M.-Y., & Wang, X.-G. 2019, ApJ, 884, 61
Eichler, D., Livio, M., Piran, T., & Schramm, D. N. 1989, Natur, 340, 126
Firmani, C., Cabrera, J. I., Avila-Reese, V., et al. 2009, MNRAS, 393, 1209
Ford, L. A., Band, D. L., Matteson, J. L., et al. 1995, ApJ, 439, 307
Geng, J. J., & Huang, Y. F. 2013, ApJ, 764, 75
Ghirlanda, G., Nava, L., & Ghisellini, G. 2010, A&A, 511, A43
Goldstein, A., Burgess, J. M., Preece, R. D., et al. 2012, ApJS, 199, 19
Golenetskii, S. V., Mazets, E. P., Aptekar, R. L., et al. 1983, Natur, 306, 451
Gruber, D., Goldstein, A., Weller von Ahlefeld, V., et al. 2014, ApJS, 211, 12
Guiriec, S., Connaughton, V., Briggs, M. S., et al. 2011, ApJL, 727, L33
Kaneko, Y., Preece, R. D., Briggs, M. S., et al. 2006, ApJS, 166, 298
Kargatis, V. E., Liang, E. P., Hurley, K. C., et al. 1994, ApJ, 422, 260
Kumar, P., & Zhang, B. 2015, PhR, 561, 1
Laros, J. G., Evans, W. D., Fenimore, E. E., et al. 1985, ApJ, 290, 728
Li, L. 2019, ApJS, 242, 16
Li, L., Geng, J.-J., Meng, Y.-Z., et al. 2019, ApJ, 884, 109
Liang, E. W., Zhang, B., O'Brien, P. T., et al. 2006, ApJ, 646, 351
Lloyd-Ronning, N. M., & Petrosian, V. 2002, ApJ, 565, 182
Lu, R.-J., Wei, J.-J., Liang, E.-W., et al. 2012, ApJ, 756, 112
Lundman, C., Pe'er, A., & Ryde, F. 2013, MNRAS, 428, 2430
MacFadyen, A. I., & Woosley, S. E. 1999, ApJ, 524, 262
Meng, Y.-Z., Liu, L.-D., Wei, J.-J., et al. 2019, ApJ, 882, 26
Narayan, R., Paczynski, B., & Piran, T. 1992, ApJL, 395, L83
Narayana Bhat, P., Meegan, C. A., von Kienlin, A., et al. 2016, ApJS, 223, 28
Norris, J. P., Marani, G. F., & Bonnell, J. T. 2000, ApJ, 534, 248
Norris, J. P., Nemiroff, R. J., Bonnell, J. T., et al. 1996, ApJ, 459, 393
Norris, J. P., Share, G. H., Messina, D. C., et al. 1986, ApJ, 301, 213
Oganesyan, G., Nava, L., Ghirlanda, G., & Celotti, A. 2018, A&A, 616, A138
Oganesyan, G., Nava, L., Ghirlanda, G., Merlandri, A., & Celotti, A. 2019, A&A, 628, A59
Paczynski, B. 1986, ApJL, 308, L43
Paczynski, B., & Xu, G. 1994, ApJ, 427, 708
Pe'er, A. 2019, arXiv:1902.02562
Pe'Er, A., & Ryde, F. 2017, IJMPD, 26, 1730018
Peng, Z. Y., Ma, L., Zhao, X. H., et al. 2009, ApJ, 698, 417
Preece, R. D., Briggs, M. S., Mallozzi, R. S., et al. 1998, ApJL, 506, L23
Preece, R. D., Briggs, M. S., Mallozzi, R. S., et al. 2000, ApJS, 126, 19
Ravasio, M. E., Ghirlanda, G., Nava, L., & Ghisellini, G. 2019, A&A, 625, A60
Rees, M. J., & Meszaros, P. 1994, ApJL, 430, L93
Ryde, F., & Svensson, R. 1999, ApJ, 512, 693
Uhm, Z. L., & Zhang, B. 2014, NatPh, 10, 351
Uhm, Z. L., & Zhang, B. 2016, ApJ, 825, 97
Uhm, Z. L., Zhang, B., & Racusin, J. 2018, ApJ, 869, 100
Ukwatta, T. N., Dhuga, K. S., Stamatikos, M., et al. 2012, MNRAS, 419, 614
Vereshchagin, G. V. 2014, IJMPD, 23, 1430003
Woosley, S. E. 1993, ApJ, 405, 273
Woosley, S. E., & Bloom, J. S. 2006, ARA&A, 44, 507
Yu, H.-F., Dereli-Bégué, H., & Ryde, F. 2019, ApJ, 886, 20
Yu, H.-F., Preece, R. D., Greiner, J., et al. 2016, A&A, 588, A135
Zhang, B. 2011, CRPhy, 12, 206
Zhang, B. 2018, The Physics of Gamma-Ray Bursts by Bing Zhang (Cambridge: Cambridge Univ. Press)
Zhang, B., Lu, R.-J., Liang, E.-W., et al. 2012, ApJL, 758, L34
Zhang, B., & Mészáros, P. 2002, ApJ, 581, 1236
Zhang, B., & Yan, H. 2011, ApJ, 726, 90
Zhang, B.-B., Uhm, Z. L., Connaughton, V., et al. 2016, ApJ, 816, 72
Zhang, B.-B., Zhang, B., Liang, E.-W., et al. 2011, ApJ, 730, 141